CZECH TECHNICAL UNIVERSITY IN PRAGUE

Faculty of Civil Engineering

Department of Mechanics

Constitutive Model for Timber Fracture Under Tension-Shear Stress States

Konstitutivní model pro porušení dřeva trhlinami při namáhání tahem a smykem

DOCTORAL THESIS

Ing. Eliška Šmídová, MSc.

Doctoral study programme: Structural Engineering

Branch of study: Physical and Material Engineering

Doctoral thesis tutor: prof. Ing. Petr Kabele, Ph.D.
doc. Ing. Lenka Melzerová, Ph.D.

Prague, 2021

CZECH TECHNICAL UNIVERSITY IN PRAGUE
Faculty of Civil Engineering
Thákurova 7, 166 29 Praha 6

DECLARATION

Ph.D. student's name: Eliška Šmídová

Title of the doctoral thesis: Constitutive Model for Timber Fracture under Tension-Shear Stress States

I hereby declare that this doctoral thesis is my own work and effort written under the guidance of the tutor Prof. Ing. Petr Kabele, Ph.D.
All sources and other materials used have been quoted in the list of references.

The doctoral thesis was written in connection with research on the project:
GAČR grant No. 18-05791S,
SGS20/155/OHK1/3T/11,
SGS17/168/OHK1/3T/11,
SGS16/038/OHK1/1T/11
SGS15/031/OHK1/1T/11
SGS14/029/OHK1/1T/11
SGS13/034/OHK1/1T/11

In Prague on 30.11.2021

signature

Acknowledgements

I would like to thank my supervisor prof. Ing. Petr Kabele, Ph.D. for proposing the topic of this Ph.D. thesis, for ideas he came up with and for his willingness to help with any problem that arose. Also, I would like to thank prof. Ing. Michal Šejnoha, Ph.D. for the opportunity to collaborate, his useful help, and sharing experience regarding the experimental campaign. In addition, I would like to thank Červenka Consulting s.r.o. for providing the development version of ATENA® finite element software. Last but not least, I would like to thank my family and friends for their devoted social and financial support.

Abstract

Timber and engineered wood products range among the most frequently used ancient and modern building materials that are friendly to environment and energy efficient with low handling costs. A suitable constitutive model, being able to capture complexity of timber behavior under various stress states, would enable more efficient design of timber structures.

This doctoral thesis first provides an overview of typical timber behavior and current timber models together with comparison of suitable failure criteria. Then, the 2D homogeneous orthotropic constitutive model for tensile and shear fracture in timber, which has been enhanced, elaborated, and implemented in a finite element method code by the author, is described. In the model, timber is considered as a 2D homogeneous continuum. The model aims at capturing fracture under tension, shear, and their combination, while taking into account the phenomena of the elastic and inelastic behavior in an infinitesimal deformation range, material orthotropy, both in linear and non-linear range, cracking across and along fibers, and the behavior under unloading/reloading. Non-linear response under combination of compression and shear is considered as a perfectly plastic. The model for the non-linear behavior is based on the cohesive crack concept. Thus, the model is composed of: (1) orthotropic failure criterion, (2) crack-type criterion, and (3) cohesive (traction-separation) law for a crack along or across the grain.

The results from an experimental campaign on solid and glued laminated timber (GLT) made of European spruce (Picea abies) with 10.5 mm or 45 mm thick lamellas are presented. The campaign included off-axis tension and compression tests, shear block test, compact tension test, and three-point bending test on notched beams and arches. The main purpose of the study was to obtain a consistent set of material parameters suitable for the calibration of a material model capable of capturing complex timber behavior, i.e. both linear and non-linear response together with respective fracture pattern, under various combinations of tension, shear, and compression in various directions of the timber axes of orthotropy. With regard to the specimens' dimensions and presence of flaws, the results from tension, compression, shear, and compact tension tests represent properties of a clear wood or GLT material while those obtained in three-point bending tests of beams and arches capture the complexity of timber fracture and provide data for the proposed model validation and further numerical simulations.

The methodology of the model calibration is described. Elastic parameters and strengths parallel and perpendicular to the grain were retrieved directly from off-axis tension and compression tests. Shear strength was calculated in the scope of the calibration of the failure surface using off-axis tension and compression test results. The crack-type criterion was calibrated based on visual inspection of off-axis tension specimens' failure. The traction-separation relation and fracture energy for the crack parallel to the grain were obtained by inverse analysis of compact tension test.

For the purpose of the model validation,

the numerical analysis of the three-point bending test of glued laminated timber arches with the fibers aligned with the longitudinal direction was carried out. The numerical results show that the model can adequately simulate the quantitative response of the arches, including the linear and non-linear behavior. Furthermore, the model captures well the most distinctive features of the cracking parallel to the grain.

The proposed constitutive model of the tensile-shear fracture in timber was also used for numerical predictions. The numerical results show that the model can adequately reproduce both the experimental load-displacement response and the crack pattern, which in certain cases comprises of cracking parallel or perpendicular to the grain. Furthermore, the results confirm that the value of the shear strength, obtained from ASTM shear test as the maximum attained force divided by the shearing area, represents the averaged stress at the failure plane, while the extreme stress experienced by the material is much higher.

Keywords: non-linear finite element analysis, orthotropic elasticity, glued laminated timber, Tsai-Hill failure criterion, shear test, 2D constitutive model, traction-separation law, smeared crack model, tensile-shear fracture, solid timber, three-point bending, single edge notched beam, single edge notched arch, off-axis tension test, off-axis compression test, compact tension test.

Abstrakt

Dřevo a dřevěné materiály se řadí mezi nejčastěji používané konstrukční materiály dob minulých i současnosti, které nezatěžují životní prostředí a jsou energeticky úsporné s nízkými náklady. Vhodný konstitutivní model, který by zachycoval složité chování dřeva při různých stavech napětí, by umožnil efektivnější návrh dřevěných konstrukcí.

Tato doktorská práce nejprve poskytuje přehled typického chování dřeva a existujících materiálových modelů spolu se srovnáním vhodných podmínek porušení dřeva. Dále práce popisuje dvourozměrný homogenní konstitutivní model porušení dřeva trhlinami pro zatížení tahem a smykem, který autorka rozšířila, rozpracovala a implementovala do konečně-prvkového kódu. V tomto modelu se dřevo idealizuje jako dvourozměrné homogenní kontinuum. Model zachycuje porušení při namáhání tahem, smykem nebo jejich kombinací, přičemž zohledňuje elastické a neelastické chování v oblasti infinitezimálních deformací, ortotropii materiálu v lineární i nelineární oblasti, vznik trhlin přes a podél vláken a chování při odtěžování a přitěžování. Nelineární odezva při kombinaci zatížení tlakem a smykem je uvažována jako dokonale plastická. Tento model popisující nelineární chování je založený na konceptu kohezivní trhliny. Tudíž se tento model skládá z: (1) ortotropní podmínky porušení, (2) podmínky typu trhliny a (3) kohezivního zákona pro trhlinu podél nebo přes vlákna.

V práci jsou prezentovány výsledky z experimentů provedených na rostlém a

lepeném lamelovém dřevě (LLD), které bylo vyrobeno ze Smrku ztepilého (Picea abies) s tloušťkou lamely 10, 5 mm nebo 45 mm. Experimenty zahrnují tahové a tlakové zkoušky se sklonem vláken, smykovou zkoušku, zkoušku CT vzorku v excentrickém tahu a zkoušku přímého nosníku s vrubem a oblouku s vrubem v tříbodovém ohybu. Cílem této experimentální části bylo získat konzistentní soubor materiálových parametrů vhodných pro kalibraci materiálového modelu, který by zachycoval složité chování dřeva, a to lineární i nelineární odezvu spolu s odpovídajícím způsobem porušení, při různých kombinacích tahového, smykového a tlakového namáhání v různých osových směrech ortotropie dřeva. S ohledem na velikost vzorků a přítomnost vad, výsledky tahových, tlakových, smykových a CT zkoušek reprezentují vlastnosti bezvadého dřeva nebo LLD, zatímco výsledky ze zkoušek nosníků a oblouků v tříbodovém ohybu zachycují složitost porušení dřeva a poskytují data pro validaci navrženého modelu a další numerické simulace.

Metodologie kalibrace modelu je popsána. Elastické parametry a pevnosti podél vláken a přes vlákna byly získány přímo z tahových a tlakových zkoušek se sklonem vláken. Smyková pevnost se vypočítala v rámci kalibrace plochy porušení za použití výsledků z tahových a tlakových zkoušek se sklonem vláken. Podmínka typu trhliny se kalibrovala na základě vizuálního posouzení porušení tahových vzorků se sklonem vláken. Kohezivní vztah a lomová energie pro trhlinu podél vláken byly získány inverzní analýzou výsledků zkoušky CT vzorku v excentrickém tahu.

Numerická analýza zkoušky oblouku s vrubem v tříbodovém ohybu byla provedena za účelem validace modelu. Oblouk byl vyroben z lepeného lamelového dřeva s vlákny rovnoběžnými s podélnou osou oblouku. Numerické výsledky ukazují, že model umí adekvátně simulovat kvantitativní odezvu oblouků, vč. lineárního i nelineárního chování. Navíc, model zachycuje odpovídajícím způsobem hlavní vlastnosti porušení trhlinami podél vláken.

Navržený konstitutivní model namáhání dřeva v tahu a smyku byl také použitý pro numerické predikce. Jejich výsledky ukazují, že model je schopen odpovídajícím způsobem reprodukovat jak experimentální odezvu zatížení vs. posun, tak způsob porušení, který v některých případech zahrnuje trhlinu podél vláken nebo přes vlákna. Výsledky navíc potvrzují, že hodnota smykové pevnosti, která byla vypočtena na základě ASTM smykové zkoušky jako maximální dosažená síla dělená smykovou plochou, představuje zprůměrované napětí na ploše porušení, zatímco největší napětí přenášené materiálem je výrazně větší.

Klíčová slova: nelineární konečně-prvková analýza, ortotropní elasticita, lepené lamelové dřevo, Tsai-Hillovo kritérium porušení, smyková zkouška, 2D konstitutivní model, zákon koheze, model fiktivní rozetřené trhliny, porušení při namáhání tahem a smykem, rostlé dřevo, tříbodový ohyb, přímý nosník s vrubem, oblouk s vrubem, tahová zkouška se sklonem vláken, tlaková zkouška se sklonem vláken, zkouška CT vzorku v excentrickém tahu.

Contents

Figures

Tables

Chapter 1

Introduction

1.1 Motivation

Timber and engineered wood products, such as laminated veneer lumber (LVL), cross-laminated timber (CLT), or glued laminated timber (GLT), represent ones of the most frequently used building materials. They are typical for low handling costs, friendliness to environment, and energy efficiency.

Structural analysis for design of timber frames and trusses is commonly based on the assumption that members are linear elastic until failure. The influence of deformations in connections is taken into account through their effective stiffness or through the prescribed slip values as a function of the load level in the connection [20]. The timber stiffnesses and strengths are obtained experimentally from bending or direct tension/compression tests on full cross-section pieces [19]. The stiffness and the load-carrying capacity of the connections are determined either by code rules [20] or from tests [21, 22, 23, 24]. The analysis is often done using the finite element method (FEM), in which case 1D elements (type beam or truss) are typically used to model the members.

However, there exists a range of special applications, in which the mechanical behavior of timber or wood products needs to be represented under more complex multiaxial and, possibly, non-proportionally evolving stress states. These applications include, e.g., optimization and verification of novel members or connections, evaluation of historic structures and connections

[25, 26, 27], and forensic analysis. In these cases, the material should be modeled as 2D or 3D continuum with appropriate failure condition and treatment of post-failure behavior. To this end, elasticity, plasticity, and fracture models, or their combination, are being used [4, 5, 7, 8, 10, 28, 29]. Since these models must describe the failure and post-failure behavior under general stress states, their calibration and validation require data from material tests performed under various stress paths, while taking into account the inherent material anisotropy. Although many experimental studies on mechanical properties of timber or wood products are reported in literature, many of them focus on a behavior under specific loading scheme or failure mode [12, 13, 30, 14, 31, 32, 33, 34]. [35]

Therefore, it is difficult to find a comprehensive set of data that would encompass, for the same material, the pre- and post-failure behavior under tension, shear, and compression and in various directions with respect to the timber axes of orthotropy. To fill this gap, we carried out an experimental program including off-axis tension and compression tests, shear block tests, compact tension (CT) tests, and three-point bending (3PB) tests of single edge notched beams and arches. As the material, we selected solid and glued laminated timber made of European spruce (Picea abies), which is widely used in the European construction sector. [35]

This work focuses on modeling of timber under multiaxial stress states where timber is considered as 2D or 3D continuum. Utilization of the experimental results is demonstrated by the calibration of a tensile-shear fracture model, which has been enhanced, elaborated, implemented in finite element software, and validated by the author in [15, 36].

1.2 Objectives

This doctoral thesis has the following objectives:

- to enhance, elaborate, and implement in a finite element program the constitutive model for fracture of timber, the foundations of which were laid in the author's master thesis,
- to acquire experimental data for model calibration and validation,
- to demonstrate the methodology of the model calibration using the obtained data,

- to validate the model and demonstrate its capacity to predict the fracture behavior of timber under complex loading states.

1.3 Organization of the doctoral thesis

- Chapter 1: Introduction,
- Chapter 2: Mechanical properties, modeling, and failure criteria of timber - state of the art,
- Chapter 3: Constitutive model for timber under tension and shear,
- Chapter 4: Experimental campaign and results,
- Chapter 5: Calibration of the constitutive model,
- Chapter 6: Validation of the model,
- Chapter 7: Predictive numerical analyses,
- Chapter 8: Conclusion.

In Chapter 1, the motivation, objectives, and structure of this work is described. Chapter 2 follows with a review of mechanical properties of timber, approaches to its modeling, failure criteria and their comparative study. Chapter 3 depicts constitutive model of tensile-shear fracture of timber recently enhanced, elaborated, and implemented in finite element software by the author. Chapter 4 describes the goals, methods, and results of the conducted experimental campaign. Chapter 5 concerns the process of model calibration using the experimental data from Chapter 4. In Chapter 6, validation of the constitutive model against experimental data of timber notched arch is discussed. Chapter 7 reports on the use of the model for predictive numerical analysis of ASTM shear test and pre-stressed compact tension test. In Chapter 8, the important ideas and results of this doctoral thesis are summarized.

Chapter 2

Mechanical properties, modeling, and failure criteria of timber - state of the art

In this chapter, mechanical properties of timber and state of the art of the approaches to its modeling are reviewed. Also, failure criteria suitable for timber are summarized and compared using available experimental data. Most of the text in this chapter was adapted from [35, 37].

2.1 Timber and its mechanical properties

Timber and its derived engineered products typically exhibit orthotropic mechanical behavior. Sawn timber has three mutually perpendicular axes in which different properties can be distinguished: longitudinal (parallel to the grain), radial (perpendicular to the grain), and tangential. Stiffness and strength related to the longitudinal direction substantially exceed those associated with the other two directions [38]. [35]

Under tensile and shear loading, the behavior of timber is nearly linear-elastic up to failure, which occurs in the form of brittle or quasi-brittle fracture, see Fig. 2.1 for tensile loading. Tension parallel to the grain usually results in a complex cracking pattern, which involves disintegration between the fibers as well as their rupture. In Fig. 2.2, the common types of timber failure in tensile tests with load acting along the grain are depicted. On the other hand, tension perpendicular or oblique to the grain typically induces

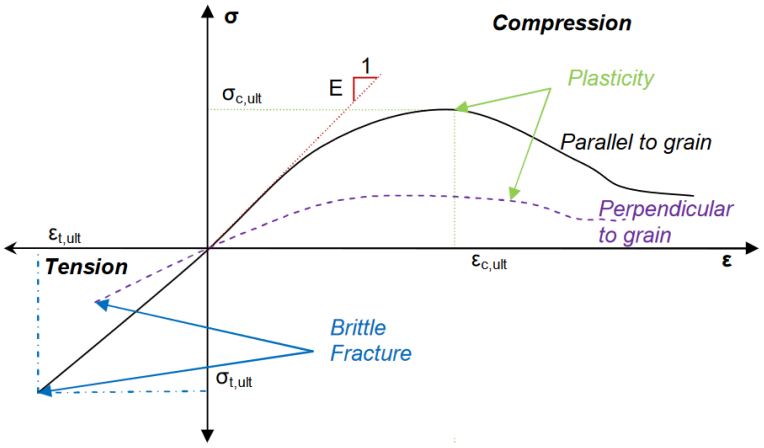

Figure 2.1: Typical stress strain behavior of timber (adapted from [1]).

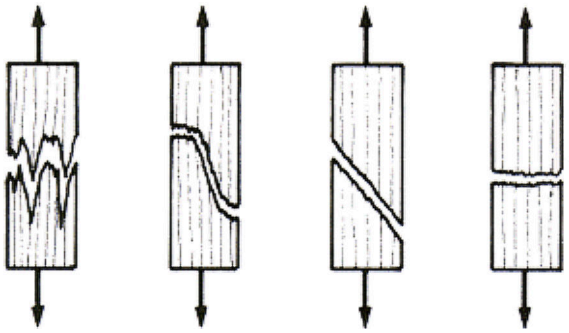

Figure 2.2: Common types of failure in timber under tensile load acting along the grain (from left to right): failure in splinter, combined tension and shear, shear, and brittle tension. [2]

cracking parallel to the grain. Similar patterns can be seen even in laminated products, provided a glue with a sufficient strength, which prevents the interlaminar failure, is used. Failure due to shear stress is characterised by sliding of fiber layers or bundles parallel to the grain. Compression stress applied parallel to the grain leads to elastic and plastic deformations with a ductile failure, often occurring in the form of so-called kink bands. All typical failure modes for such compression test configuration are depicted in Fig. 2.3. Compression stress perpendicular to the grain induces a ductile failure with plastic deformations in the form of fibers' crushing [4, 39]. More details about non-elastic properties of timber can be found e.g. in [40]. [35]

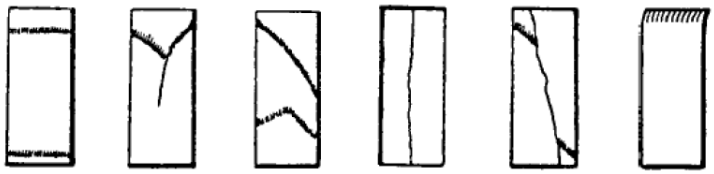

Figure 2.3: Common types of failure in timber under compressive load acting along the grain (from left to right): crushing, wedge split, shearing, splitting, compression and shearing parallel to the grain, brooming or end-rolling. [3]

2.2 Modeling of timber

The main subject of the thesis is modeling of timber behavior under complex multiaxial stress states, which is required e.g. for optimization and verification of novel members or connections. Therefore, we narrow the forthcoming review to models, which idealize the material as 2D or 3D continuum and account for its failure by adopting appropriate failure condition and treatment of its post-failure response. To this end, elasticity, plasticity, and fracture models, or their combination are being used.

2.2.1 Micro-macro model of earlywood and latewood layers

In the work of Holmberg et al. [4], the mechanical behavior of wood was studied from a micro up to a macro level. The continuum properties, such as stiffness and shrinkage, were derived by use of a homogenization procedure and the finite element method. For the purpose of numerical simulations of the deformation and fracturing of wood specimens loaded under conditions similar to those found in the refining process, a constitutive model distinguishing earlywood and latewood zones in the growth ring was developed. Crushable foam model, based on non-associated compressible plasticity, was used for the earlywood layer behavior [41]. For the latewood, the non-linear fracture mechanics model was employed using the fictitious crack model [42]. It was implemented by introducing special crack elements. Based on experimental results, softening stress-relative displacement relations for pure opening and shearing modes (mode I and II) were approximated by bi-linear curves. Two specimen types were described: the wood subjected to shear loading in tangential and radial direction, see Fig. 2.4.

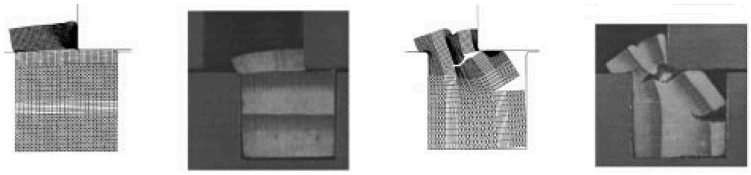

(a) (b)

Figure 2.4: Comparison between numerical simulation and experimental results: loading in (a) the tangential and (b) the radial direction. [4]

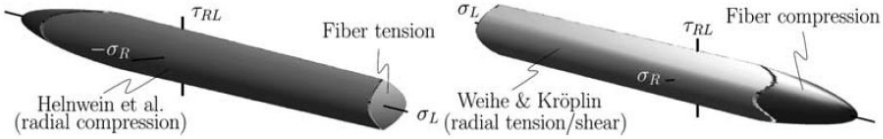

Figure 2.5: Initial state of the multi-surface wood model in the plane stress orthotropic stress space.[5]

2.2.2 Multi-surface plasticity model

Based on bi-axial experiments of spruce wood, Mackenzie et al. [5] described mechanical behavior of clear wood by means of multi-surface plasticity model. It consists of four surfaces, each stands for one basic failure mode: (1) modified tension cut-off for fiber rupture, (2) mixed mode radial tension-shear model by Weihe [43] applied to the perpendicular to the grain direction, (3) an extension of the author's prior model for perpendicular to grain compression [44], and (4) the compressive failure parallel to grain. The initial state of the four yield conditions (failure envelopes) is shown in Fig. 2.5 with respect to the stress parallel to the grain (σ_L), radial stress (σ_R), and shear stress (τ_{RL}). The model was used for the analysis of a cross-wise joint of two wooden rods. Similarly as the single-surface elliptic failure envelope of Tsai and Wu [45], the introduced multi-surface model reproduces well the failure stress states obtained in bi-axial experiments. The numerical implementation of the multi-surface is simplified compared to single-surface failure envelope thanks to the possibility to attribute to each of the surfaces a relevant failure mode and the respective post-failure behavior. On the other hand, the multi-surface softening plasticity model requires to tackle the stability at larger time steps.

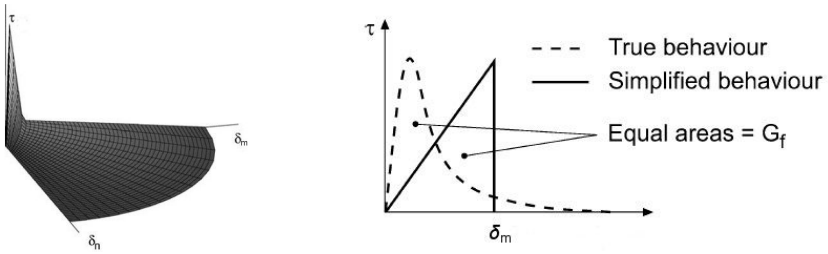

(a) (b)

Figure 2.6: Approximation used in (a) fictitious crack model: shear stress (τ) as a function of shear slip (δ_m) and opening displacement (δ_n) [6] and (b) quasi non-linear fracture mechanics: shear stress (τ) as a function of shear slip (δ_m). [7]

2.3 Linear-elastic and non-linear fracture mechanics models

The paper of Serrano and Gustafsson [7] discusses a few fracture mechanics strength analysis methods recently proposed in relation to timber engineering strength design. The methods are based either on linear elastic fracture mechanics (LEFM) or non-linear fracture mechanics (NLFM). In LEFM, a pre-existing crack with accompanying square root stress singularities is considered and failure criterion is defined in terms of energy release during the crack propagation or stress intensity factor (K). Critical energy release rate (G_c) or critical stress intensity factor (K_c) characterise the material. The NLFM approach, developed from the principles of Hillerborg's fictitious crack model [42], considers stress transfer beyond the maximum stress point in the form of strain softening of stress-crack opening displacement (COD) relation (diminishing stress at increasing COD) for the material. Shear stress is formulated as a function of opening and shear slip across the bond line. The shear stress surface is shown in Fig. 2.6a. Other discussed approaches are generalised LEFM [46], which does not use pre-existing crack for analysis, and quasi-non-linear fracture mechanics approach [47, 48], in which the deformation of the fracture process region is considered only by a linear elastic stress-COD relation, see Fig. 2.6b. The slope of the linear elastic relation is defined so as the area beneath it is equal to the the fracture energy (G_f) of the material. Examples of numerical applications are presented for structural components, dowel joints, and adhesive joints.

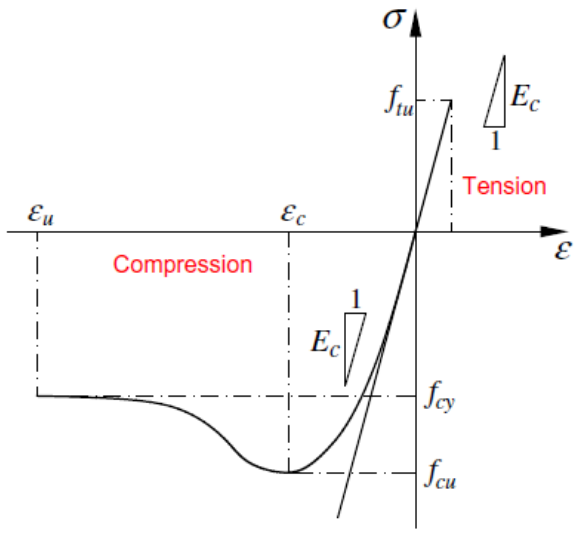

Figure 2.7: The frame FE approach: the adopted stress–strain relationship. [8]

2.3.1 Frame finite element approach

In the work of Valipour and Crews [8], development and application of the frame finite element (FE) is presented. The approach is considered simple and efficient, compared with more complex and computationally demanding FEs, and suitable for parametric studies applied in design. The method was applied to estimate the load-carrying capacity of timber beams flexurally strengthened with externally bonded fiber reinforced polymer strips and near-surface mounted FRP bars. The frame FE is able to capture timber crushing under compression and timber fracture under tension and FRP rupture. For compression, stress-strain law presented by Glos [49] was used. Tension behavior was assumed linear elastic with brittle failure. Both laws are shown in Fig. 2.7 where f_{cu} and ε_c are the ultimate compressive strength with corresponding strain, f_{cy} is the residual stress, E_c is the initial elastic modulus of timber in compression and f_{tu} is tensile strength.

The model was developed in the framework of a flexibility-based fiber element formulation. To take account of shear-slip, novel method based on central difference method in conjunction with composite Simpson's integration scheme along the element axis was proposed.

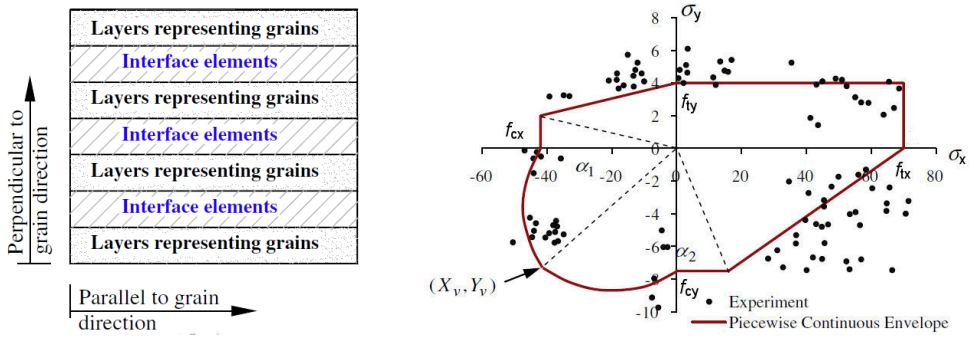

Figure 2.8: Outline of the model: (a) layered approach used for orthotropic behaviour of timber and (b) proposed piecewise continuous orthotropic failure envelope for a spruce wood specie based on bi-axial experiments by Eberhardsteiner et al. [9]. [10]

2.3.2 The layered approach and hypoelastic constitutive law

The paper of Khorsandnia et al. [10] treats the development and application of continuum-based finite element modeling approach to non-linear orthotropic behavior of timber, timber–concrete composite (TCC) beams and joints. In the model, timber is considered as a composite material with timber grain layers that are connected to each other by interface elements (Fig. 2.8a).

The timber behavior along the grain is described by the piecewise continuous failure envelope proposed in the bi-axial stress space, see Fig. 2.8b where σ_x and σ_y are normal stresses, f_{tx} and f_{ty} are the tensile strengths, and f_{cx} and f_{cy} are the compressive strengths parallel and perpendicular to the grain. (X_v, Y_v) define the location of failure envelope vertex. The hypoelastic constitutive law and equivalent uniaxial strain concept are used for the failure surface formulation. The equivalent uniaxial stress–strain diagram is adopted for timber grain. It considers a linear softening branch for timber under tension and compression and the unloading/reloading follows the total secant line to the origin. The softening of material is treated by the concept of a failure band approach.

The interface elements capture the behavior of timber perpendicular to the grain and their stiffness and strength is determined based on mechanical properties in the direction perpendicular to the grain. They can only capture the linear elastic–brittle failure behaviour under tension.

2.3.3 Plasticity-damage model

Xu et al. [28] proposed a 3D non-linear finite element model to describe the timber behavior. For stress states in compression, they used anisotropic elasto-plastic constitutive law with hardening following the Hill's yield criterion [50]. For brittle behavior under tension and shear, the modified Hill's failure criterion was applied. In this criterion, the progressive failure is simulated by reducing the material modulus to represent the damage evolution. The model reproduced well the experimental measurements of embedding strength of glued laminated timber for dowel-type fasteners.

2.4 Failure criteria

To predict load capacity of timber structural members subjected to multiaxial loading, failure criteria containing minimum input material parameters from simple material tests are needed. Various phenomenological failure criteria have been proposed. Although they do not clarify the failure mechanism, they identify whether failure occurs or not. Many of the non-isotropic criteria designed for composite materials [51, 52, 53] are applicable also for the orthotropic material of wood. Used with numerical models, they are considered appropriate to assess failure of wood members [54, 55, 56, 57]. Phenomenological strength criteria for wood describe a surface with constraints ensuring that the surface is closed. Furthermore, using the orthotropic plasticity, stress analyses of wood materials beyond the elastic limit (post-failure analysis) can be performed. Some criteria were developed directly for wood [58, 59].

A few studies that compared failure criteria against experimental results on timber have been conducted. In [60], the current state of the art in applying phenomenological failure criteria to wood and wood-based materials was summarized. In [61], existing phenomenological strength criteria with known uniaxial strength values were applied to clear wood data to predict failure of biaxial tests. The best results were obtained for Norris [58], quadratic [62], Tsai-Hill [63], and van der Put criteria [59]. There, the following conclusion was drawn: a general criterion should be chosen with respect to the biaxial stress state.

2.5 Comparative study of failure criteria

In order to select the most appropriate failure criterion for our model, we compared four existing failure criteria: (1) Lourenco's criterion modified for wood by the author [40, 15], (2) Tsai-Hill criterion [58], (3) Hankinson's formula [64] and (4) Hyperbolic formula [65]. Furthermore, we applied some of the modifications of the Lourenco's criterion to the other criteria. We made the comparison against the data available in the literature for Sitka spruce, Katsura [11], Douglas fir [12], Douglas fir laminated veneer [13] and Cupiúba [14]. The study was originally published by the author [37] and its main parts are extracted below.

The failure formulas are expressed in terms of 2D plain stress state in the uniaxial tensile test with various load-grain angle θ, see Fig. 5.1. The applied force P produces stress $\boldsymbol{\sigma}' = \{\sigma_{x'}, \sigma_{y'}, \tau_{x'y'}\}^T$ referenced to the $x' - y'$ system of coordinates. Stress and strain vectors can be transformed to the material coordinate system $x-y$ by pre-multiplying them with the appropriate transformation matrix, see Eq. (5.2). In the formulas, f_{xy} is an absolute value of the shear strength, f_{tx} and f_{ty} are the tensile strengths, and f_{cx} and f_{cy} are the compressive strengths parallel and perpendicular to the grain, respectively, c is $\cos\theta$ and s is $\sin\theta$, σ^F denotes the axial stress at failure.

2.5.1 Lourenco's criterion modified for timber

Failure criterion that has been proposed by the author in [15] is defined by means of Rankine failure surface modified for orthotropy [66]. It is further enhanced by (1) calibration parameter p_s that multiplies shear strength f_{xy} and (2) shear strength as an upper bound of the shear stress τ_{xy}. The enhancements enable calibration of the failure surface through off-axis test results. Failure occurs if the stress state $\boldsymbol{\sigma}$ reaches the failure surface $\tau_{xy,f_{xy}}(\sigma_x, \sigma_y)$:

$$\tau_{xy} = \tau_{xy,f_{xy}}(\sigma_x, \sigma_y) \tag{2.1}$$

$$\tau_{xy,f_{xy}}(\sigma_x,\sigma_y)=\begin{cases}\frac{p_s f_{xy}}{f_{tx}f_{ty}}\sqrt{f_{tx}f_{ty}(\sigma_x-f_{tx})(\sigma_y-f_{ty})} \\ \qquad \text{for } \tau_{xy}<f_{xy} \\ f_{xy} \\ \qquad \text{for } \tau_{xy}\geq f_{xy}\end{cases} \tag{2.2}$$

2.5.2 Tsai-Hill criterion

The most frequently used failure theory for wood was proposed by Norris [58]. It is also referred to as the Tsai-Hill criterion. It is an extension of the von Mises-Hencky distortion energy hypothesis:

$$\left(\frac{\sigma_x}{f_{tx}}\right)^2-\frac{\sigma_x\sigma_y}{f_{tx}f_{ty}}+\left(\frac{\sigma_y}{f_{ty}}\right)^2+\left(\frac{\tau_{xy}}{f_{xy}}\right)^2=1 \tag{2.3}$$

2.5.3 Hankinson's formula

This formula [64] has been used mostly for predicting the ultimate compressive strength of wood. Some researchers have applied it also for predicting tensile strength [67]. The formula involves a parameter h:

$$\sigma^F(\theta)=\frac{f_{tx}f_{ty}}{f_{tx}s^h+f_{ty}c^h} \tag{2.4}$$

2.5.4 Hyperbolic formula

The hyperbolic formula has been developed to provide a better fit to Douglas Fir off-axis test results compared to other commonly used failure theories [65]:

$$\sigma^F(\theta) = \frac{2 f_{tx} f_{ty}}{exp^{0.01\theta}(f_{tx} + f_{ty}) + exp^{-0.01\theta}(f_{ty} - f_{tx})} \tag{2.5}$$

2.5.5 Results and discussion

Using the transformation of stress from the global coordinates x' - y' to the material ones x - y in Eq. (5.2), the failure criteria are expressed in terms of axial stress at failure with respect to off-axis angle $\sigma^F(\theta)$ and compared with the experimental data from the literature for off-axis tensile and shear tests. For the purpose of calibration, two enhancements of the Lourenco's failure criterion proposed by the author (Section 2.5.1) are applied to the other failure conditions, if possible. These are:

1. shear strength multiplier p_s in the failure surface formula,
2. shear strength as an upper bound of shear stress in a 2D stress space.

Sitka spruce and Katsura

Yoshihara and Ohta conducted off-axis tensile and shear test for Sitka spruce (Picea sitchensis Carr.) and Katsura (Cercidiphyllurn japonicurn Sieb. and Zucc.) [11]. Specimens were conditioned at 65% relative humidity. For the first experiment type, dog-bone specimens with the outer dimensions of 140 mm x 10 mm x 8 mm were cut, five pieces for each grain angle out of 0°, 5°, 10°, 15°, 20°, 25°, 30°, 45°, 60°, 75° and 90°. Shear strength was obtained from both off-axis tensile test (by transformation of the axial strength to the stress components of orthotropic symmetry) and torsion test. For the latter, ten dog-bone specimens with the outer dimensions of 180 mm x 20 mm x 5 mm were prepared. In this experimental campaign, shear strength from torsion test coincided well with that from the off-axis test for 15° - 30°.

Off-axis tensile test and shear test results for Sitka spruce together with the uncalibrated failure curves ($p_s = 1.0$, $h = 1.0$) are shown in Fig. 2.9a in terms of off-axis tensile test variables. We can see that out of the uncalibrated curves, the Tsai-Hill curve represents a good estimate. Calibrating the modified Lourenco's, Tsai-Hill and Hankinson's curves by the parameters of $p_s = 2.0$, $p_s = 1.2$ and $h = 1.8$, respectively, and activating the shear

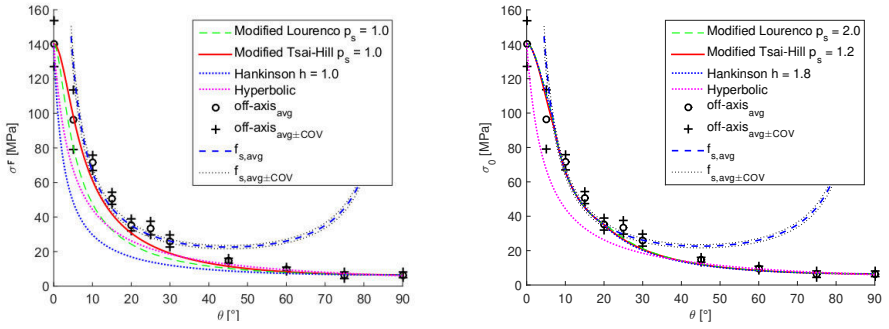

(a) (b)

Figure 2.9: The experimental data of Sitka spruce [11] with (a) uncalibrated and (b) calibrated failure conditions.

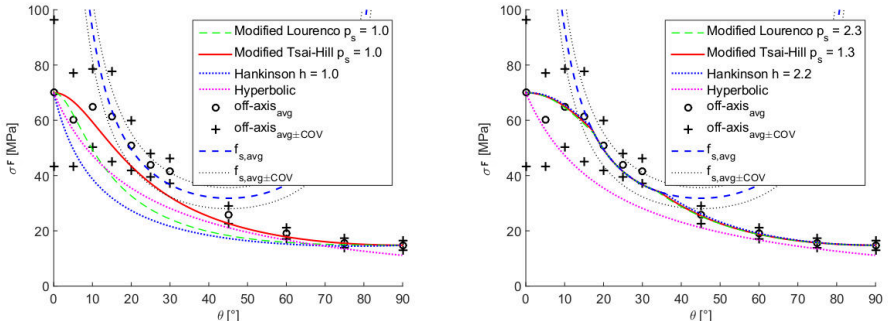

(a) (b)

Figure 2.10: The experimental data of Katsura [11] with (a) uncalibrated and (b) calibrated failure conditions.

strength upper bound, we obtain the best fit of the average experimental data, see Fig. 2.9b. On the contrary, the Hyperbolic curve does not reproduce the data well.

Experimental data for Katsura are plotted together with uncalibrated and calibrated failure curves in Fig. 2.10a and Fig. 2.10b, respectively. Similarly to the results for Sitka spruce, Tsai-Hill curve is the best estimate out the uncalibrated curves. Nevertheless, by the calibration of the modified Lourenco's, Tsai-Hill and Hankinson's curves by the parameters of $p_s = 2.3$, $p_s = 1.3$ and $h = 2.2$, respectively, and by application of the shear strength limit to the shear stress, we get a good prediction of the data. The Hyperbolic curve strongly underestimates the data.

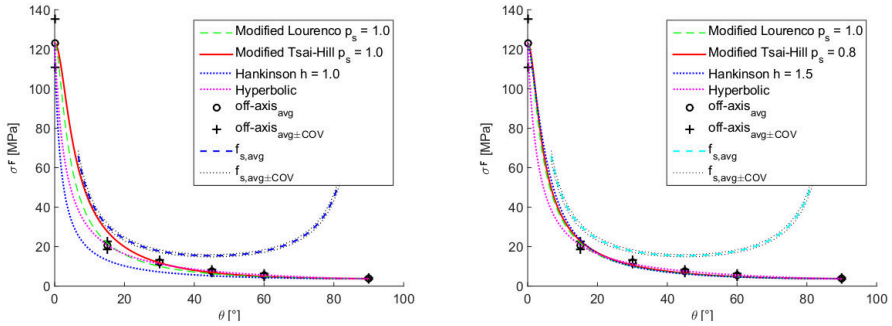

(a) (b)

Figure 2.11: The experimental data of Douglas fir [12] with (a) uncalibrated and (b) calibrated failure conditions.

Douglas Fir

Woodward and Minor measured tensile strength parallel and perpendicular to fibers and shear strength for Douglas Fir (Pseudotsuga menziesii) [12] according to the specimen configuration and testing procedure specified by ASTM D143-09 [68]. They used eight specimens for each type of experiment. For determination of the ultimate strength at grain angles of 15°, 30°, 45° and 60°, they used eight rectangular specimens for each grain angle. The specimens were 38 mm wide, 10 mm thick and they were of different length, excluding the gripping area: 480 mm, 330 mm, 250 mm and 200 mm for the grain angles of 15°, 30°, 45° and 60°, respectively. The specimens were dried to the moisture content of $12 \pm 1\%$.

Uncalibrated and calibrated failure curves are shown in Fig. 2.11a and Fig. 2.11b, respectively, together with the experimental results for Douglas fir. Both the modified Lourenco's and Hyperbolic criterion fit the average off-axis tensile test data well without any calibration. On the other hand, we can reproduce the data even better applying $p_s = 0.8$ and $h = 1.5$ to the Tsai-Hill and Hankinson's formulas. Let us note that for this wood species, the shear strength upper bound is not activated. In this study, we disregard size effect following conclusions of a related experimental work [31].

Douglas fir laminated veneer

Clouston et al. performed off-axis tensile test and shear test for Douglas fir laminated veneer [13]. Off-axis specimens of equal size (610 mm x 63 mm x 35 mm) were cut with grain angles of 0°, 15°, 30°, 45°, 60° and 90°, sixteen

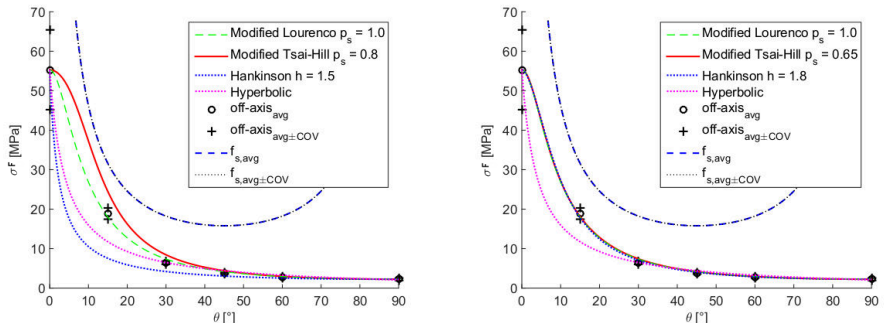

(a) (b)

Figure 2.12: The experimental data of Douglas fir laminated veneer [13] with (a) uncalibrated and (b) calibrated failure conditions.

to eighteen pieces for each angle. Shear strength was evaluated on nineteen standard ASTM shear block specimens using shear adjustment factor [69]. Average moisture content of the specimens was 7.9%. Looking at uncalibrated failure curves and experimental data in Fig. 2.12a, we can see that the modified Lourenco's curve represents the best estimate. We can get similar results if we calibrate the Tsai-Hill's and Hankinson's criteria by $p_s = 0.65$ and $h = 1.8$, respectively, see Fig. 2.12b. We can notice that the shear strength upper bound is not activated.

Cupiúba

Todeschini conducted off-axis tensile and shear test for Cupiúba (Goupia glabra) [14] in accordance with the Brasilian norm NBR 7190 [70]. For the purpose of the off-axis test, dog-bone specimens with the outer dimensions of 280 mm x 20 mm x 20 mm were cut, twelve pieces for each grain angle out of 0°, 15°, 30°, 45°, 60°, 75° and 90°. Shear strength was measured using shear block specimens. The moisture content of the specimens varied from 12% to 14%.

Plotting the uncalibrated curves together with the experimental results of Cupiúba (Fig. 2.13a), we can see that the Hyperbolic curve yields the closest estimate of the average off-axis data. Fig. 2.13b shows that we can reproduce well the data utilizing $p_s = 0.6$, $p_s = 0.4$ and $h = 1.7$ for the modified Lourenco's, Tsai-Hill and the Hankinson's criteria, respectively. Similarly to the case of Douglas fir and Douglas fir laminated veneer, the shear strength upper bound is not activated.

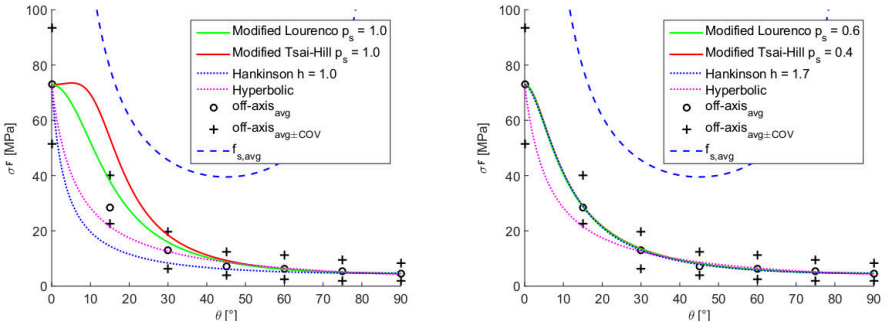

(a) (b)

Figure 2.13: The experimental data of Cupiúba [14] with (a) uncalibrated and (b) calibrated failure conditions.

2.5.6 Partial summary

Four orthotropic failure criteria were compared against off-axis and shear experimental results available in the literature for the wood species of Sitka spruce, Katsura, Douglas fir, Douglas fir laminated veneer and Cupiúba. The enhancements of the modified Lourenco's criterion, which has been proposed by the author in [15], were applied to the Tsai-Hill, Hankinson's and Hyperbolic formula, to a certain extent. Specifically, (1) the shear strength multiplier and (2) the shear strength upper bound were used. Following partial conclusions were drawn:

1. The shear strength multiplier enables calibration of a failure formula that contains shear strength. In this way, both the modified Lourenco's and Tsai-Hill criteria provide an improved estimation of the average off-axis data for Sitka spruce, Katsura, Douglas fir, Douglas fir laminated veneer and Cupiúba compared to uncalibrated criteria.

2. The shear strength upper bound, that can be activated as a maximum limit of the shear stress component for the modified Lourenco's, Tsai-Hill, and Hankinson's criteria, provide a better fit for average off-axis data of Sitka spruce and Katsura compared to these criteria without shear strength upper bound. For these wood species, average shear strength measured by torsion test coincides well with the average off-axis strength.

3. Calibration of the Hankinson's formula by the parameter h yields good estimates for all wood species involved in this study, similarly as the modified Lourenco's and Tsai-Hill criteria do. In contrast, the Hyperbolic formula predicts well only Douglas fir data as it does not contain any calibration or shear strength parameter.

Chapter 3

Constitutive model for timber fracture under tension and shear

This chapter describes the constitutive model for fracture behavior of timber under combined action of tension and shear. Foundations of the model have been laid in the author's Master thesis [40]. Within the scope of the Ph.D. study, the model has been further refined and implemented in the development version of the finite element package ATENA® [15]. The enhancements consisted mainly in the following aspects:

- The use of the Tsai-Hill failure surface [58] that distinguishes between compressive and tensile failure strengths instead of the Lourenco's failure surface [66] modified by the author.
- Implementation of perfectly plastic non-linear response under combination of compression and shear.
- Enhancement of the post-failure behavior to other than the first and the fifth octant of the 2D plane stress space, which is depicted in Fig. 3.1 for the first to fourth octant with the positive shear stress component.
- Softening behavior was prescribed for traction-separation laws in both the crack-normal ($t_n(\delta_n,\delta_m)$) and crack-tangent ($t_m(\delta_n,\delta_m)$) directions with respect to the crack-sliding displacement (δ_m). The relations are plotted in Fig. 3.2.

Most of the text in this chapter comes from the author's manuscript [35], which is presently under review for publication in a refereed journal.

As noted earlier, sawn timber typically exhibits three axes of orthotropy with regard to the natural arrangement of the growth rings along a tree trunk. In practice, especially for GLT, the overall properties in the two directions orthogonal to the grain are considered smeared as the orientation of radial and tangential axes varies among (or even within) the individual lamellas [71], as shown later e.g. in Fig. 4.6d. Accordingly, modeling is done in this work in the framework of transverse isotropy (or orthotropy in 2D), differentiating between behavior in directions parallel and perpendicular to the grain. The model idealizes timber as a 2D homogeneous continuum. It aims, in particular, at capturing fracture under tension, shear, and their combination, while taking into account the phenomena of an elastic and inelastic behavior in a small deformation range, material orthotropy, both in linear and non-linear range, cracking parallel and perpendicular to the grain, and the behavior under unloading/reloading.

The model for the non-linear behavior is based on the fictitious cohesive crack concept [42] and thus it is composed of:

- failure criterion defining the stress condition for crack initiation,
- crack-type criterion that distinguishes whether the crack occurs along or across the grain,
- cohesive (traction-separation) law defining the response of a crack.

3.1 Failure criterion

Failure (fracture) is assumed to occur when the following condition is satisfied:

$$F(\sigma_x, \sigma_y, \tau_{xy}) = 1 \tag{3.1}$$

Here σ_x, σ_y, and τ_{xy} are the stress components with respect to the axes of orthotropy. F is defined by the Tsai-Hill formulation [58] as:

$$F = \frac{\sigma_x^2}{f_x^2} - \frac{\sigma_x \sigma_y}{f_x^2} + \frac{\sigma_y^2}{f_y^2} + \frac{\tau_{xy}^2}{f_{xy}^2} \tag{3.2}$$

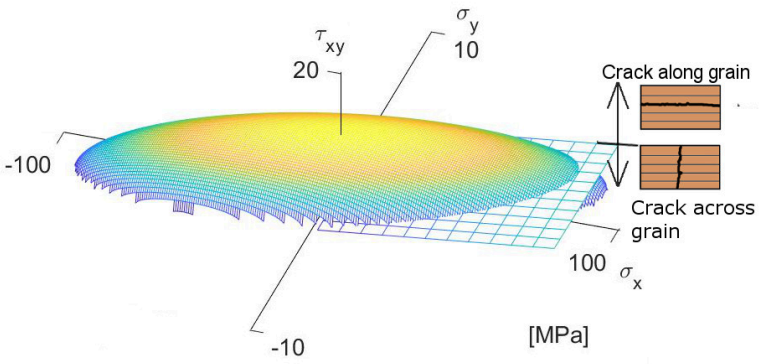

Figure 3.1: The Tsai-Hill failure surface F in 2D stress space divided by the crack type function F_{CT} into two parts.

$$\text{if } \sigma_x \geq 0 \text{ then } f_x = f_{tx} \text{ else } f_x = f_{cx} \tag{3.3}$$

$$\text{if } \sigma_y \geq 0 \text{ then } f_y = f_{ty} \text{ else } f_y = f_{cy} \tag{3.4}$$

where f_{xy} is an absolute value of the shear strength. Symbols f_x and f_y are the tensile or compressive strengths parallel and perpendicular to the grain, respectively: for the positive values of σ_x and σ_y, f_x and f_y take the tensile strength values f_{tx} and f_{ty}, respectively, otherwise the compressive strength values f_{cx} and f_{cy} are adopted. The Tsai-Hill failure surface is plotted in the 2D stress space in Fig. 3.1.

3.2 Crack-type criterion

The crack-type criterion is based on the consideration that when timber is exposed to tension in the direction parallel or nearly parallel to the grain, rupture occurs across the grain (Fig. 2.2, Fig. 4.2a, Fig. 4.2b) and the crack is idealized as perpendicular to the principal stress direction (Fig. 4.2c - Fig. 4.2e). When the angle θ, describing the deviation of the principal tension from the grain, is larger than a certain threshold (θ_c), then the crack forms along the grain regardless of the principal stress direction. To distinguish these cases, the crack-type function F_{CT}, Eq. (3.5), and criteria for cracking parallel and perpendicular to the grain, Eq. (3.6) and Eq. (3.7), are introduced:

$$F_{CT} = \left| \frac{2\tau_{xy}}{\sigma_x - \sigma_y} \right| - tan(2\theta_c) \tag{3.5}$$

$$\text{Crack across the grain: } F_{CT} < 0 \tag{3.6}$$

$$\text{Crack along the grain: } F_{CT} \geq 0 \tag{3.7}$$

As seen in Fig. 3.1, in the 2D stress space the crack-type function F_{CT} defines a plane, which divides the failure surface into two parts.

3.3 Cohesive (traction-separation) law

It is considered that the crack surfaces do not completely separate at the instant of cracking, as they may remain bridged by incompletely ruptured or debonded fibers. Using the concept of cohesive crack model [42], the bridging effect is represented by a cohesive traction acting between the crack faces. This traction gradually decreases as the crack widens, which is modeled by the traction-separation law. It relates the normal and tangent tractions, t_n and t_m, to the relative normal and tangent displacement between the crack surfaces, δ_n and δ_m. Due to its ability to fit a wide range of softening responses, the exponential form of the traction-separation law originally proposed by Hordijk [72] was adapted for the combined tension-shear traction state as follows:

$$t_n(\delta_n, \delta_m) = \begin{cases} t_n^{ci} & \left(1 - \sqrt{\frac{\delta_n^2}{\delta_{n,crit}^2} + \frac{\delta_m^2}{\delta_{m,crit}^2}}\right)\left(1 + \left(\frac{c_1\delta_n}{\delta_{n,crit}}\right)^3\right) \\ & \exp\left(\frac{c_2\delta_n}{\delta_{n,crit}}\right) - \exp\left(-c_2\right)\left(1 + c_1^3\right)\frac{\delta_n}{\delta_{n,crit}} \\ & \text{for } \delta_n \in [0, \delta_{n,crit}) \text{ and } \delta_m \in [0, \delta_{m,crit}) \\ 0 & \text{for } \delta_n \geqslant \delta_{n,crit} \text{ or } \delta_m \geqslant \delta_{m,crit} \end{cases} \tag{3.8}$$

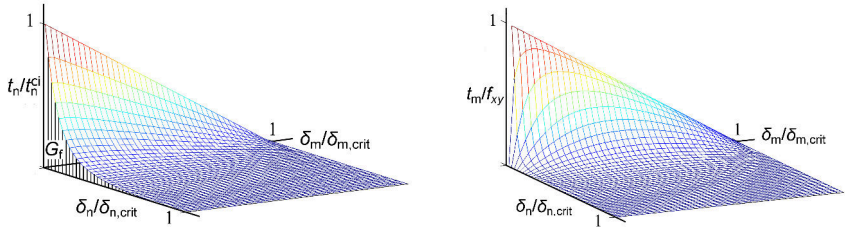

(a) (b)

Figure 3.2: Plots of cohesive law for (a) crack-normal traction $t_n(\delta_n, \delta_m)$ (Eq. (3.8)) with fracture energy G_f as an integral of $t_n(\delta_n, \delta_m)$ and (b) crack-tangent (shear) traction $t_m(\delta_n, \delta_m)$ (Eq. (3.9)) [15].

$$t_m(\delta_n, \delta_m) = \begin{cases} t_m^{ci} & \left(1 - \sqrt{\frac{\delta_n^2}{\delta_{n,crit}^2} + \frac{\delta_m^2}{\delta_{m,crit}^2}}\right) \frac{2}{\pi} \\ & \arctan\left(\frac{\delta_m}{l_{ch}} \frac{1-\left(\frac{\delta_n}{\delta_{n,crit}}\right)^p}{\left(\frac{\delta_n}{\delta_{n,crit}}\right)^p}\right) \\ & \text{for } \delta_n \in (0, \delta_{n,crit}) \text{ and } \delta_m \in (0, \delta_{m,crit}) \\ t_m^{ci} & \text{for } \delta_n = 0 \text{ and } \delta_m = 0 \\ 0 & \text{for } \delta_n \geqslant \delta_{n,crit} \text{ or } \delta_m \geqslant \delta_{m,crit} \end{cases} \tag{3.9}$$

where t_n^{ci} is the crack-normal traction at crack initiation, t_m^{ci} is the crack-tangent traction at crack initiation, c_1 and c_2 are fitting parameters defining the slope of the t_n function, $\delta_{n,crit}$ and $\delta_{m,crit}$ are the values of δ_n and δ_m, respectively, at which the cohesive traction vanishes. Parameter l_{ch} is the characteristic length of the smeared crack model related to the finite element size and p is a material parameter that determines the slope of the function t_m. The same form of the traction-separation relation is used both for cracks parallel and perpendicular to the grain, although the respective values of the parameters may be different. The plot of the traction-separation law is shown in Fig. 3.2.

It should be noted that another important characteristic, the mode-I fracture energy G_f, is related to the traction-separation law. The fracture energy G_f, which is defined as the amount of energy required to form a unit area of a traction-free crack can also be expressed by integrating the traction-separation relation along the pure-opening path (see also Fig. 3.2a):

$$G_f = \int_{\delta_n=0}^{\delta_{n,crit}} t_n(\delta_n, 0)\, d\delta_n \tag{3.10}$$

3.4 Implementation in the finite element method code

In this section, implementation of the proposed constitutive model in the development version of ATENA® finite element software, that was provided by Červenka Consulting, is described.

As the proposed model cannot be described by the standard materials or by user laws in the fracture-plastic material provided by ATENA®, a dynamic link library (DLL) was prepared in C programming language. To this end, the source of the example user DLL (CCUserMaterialExampleDLL) and ATENA® user input files included in ATENA® installation were used. The library exports several functions that will be called by the ATENA® kernel. [73]

The user project distinguishes user material parameters and user state variables. The former are properties of the material. Their values are read from an input file and they do not change during the analysis. The latter are defined separately in each material point and their main purpose is to reflect the (local) changes in the material. [73]

The applied load in non-linear analysis is divided into load steps in which a non-linear system of equations is solved by (linear) iterations, e.g. by Full Newton-Raphson method outlined in Fig. 3.3. For each iteration, a linear approximation system is built and solved. The global stiffness matrix of the linear system is built from local tangent stiffness matrices. In case of user material, the function UserDLLTangentStiff() is called for each material point to get the local matrices. The tangent stiffness matrix of the elastic-cracking material is formulated for the proposed 2D fixed smeared crack model in Section 4.5.3 in the author's master thesis [40]. [73]

The material response to a deformation increment is asked possibly multiple times in each iteration for each material point. For the user material, this has to be implemented in the function UserDLLCalculateResponse(). [73]

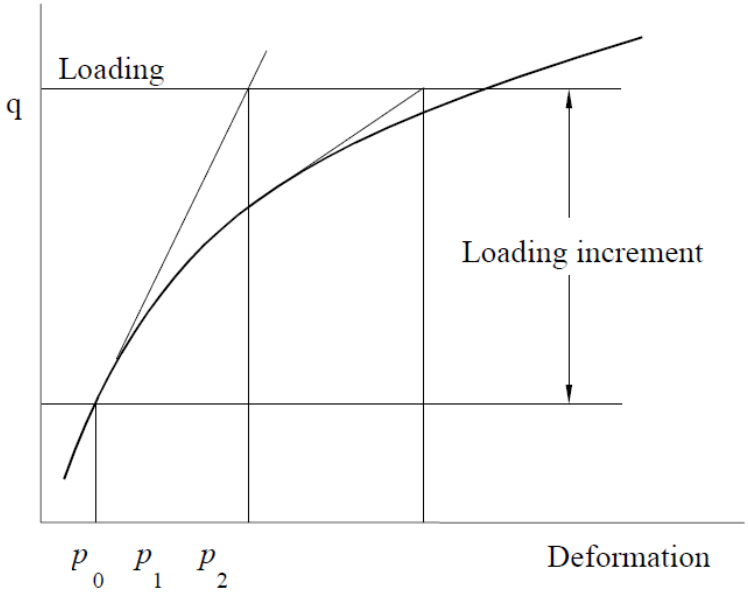

Figure 3.3: Full Newton-Raphson method. [16]

Chapter 4

Experimental campaign and results

As we claimed in Chapter 1, it is difficult to find in available literature a coherent set of experimental data that would allow us to calibrate and validate not only the proposed constitutive model but also other material models capable of capturing mechanical response of timber to complex multiaxial stress states, taking into account the failure and post-failure behavior together with the inherent material anisotropy. Although many experimental studies on mechanical properties of timber or wood products are reported in literature, many of them focus on a behavior under specific loading scheme or failure mode [12, 13, 30, 14, 31, 32, 33, 34]. [35]

Therefore, for the same material, a set of experiments the would encompass the pre- and post-failure behavior under tension, shear, and compression and in various directions with respect to the timber axes of orthotropy is needed [74]. To fill this gap, we carried out an experimental program including off-axis tension and compression tests, shear block tests, compact tension (CT) tests, and three-point bending (3PB) tests of single edge notched beams and arches. As the material, we selected solid and glued laminated timber made of European spruce (Picea abies), which is widely used in the European construction sector. Utilization of the results is demonstrated by the calibration of a tensile-shear fracture model, which has been enhanced, elaborated, and validated by the author in [15, 36]. Most of the text of this chapter is adapted from [36, 35]. [35]

4.1 Material

In this study, we used the material of solid timber and glued laminated timber made of European spruce (Picea abies) with 10.5 mm or 45 mm thick lamellas, hereinafter denoted as 10.5 mm GLT and 45 mm GLT, respectively. The tested specimens were saw-cut from larger pieces conditioned in an indoor environment with a temperature of 21° and relative humidity of 55% for 2 months. An attention was paid to produce samples that were representative elements of the GLT structure and free of defects (knots, cracks etc.). During testing, the average moisture content of the samples was 8% and the density was 463 kg/m^3.

4.2 Equipment and data acquisition

Mechanical tests were conducted in MTS Alliance RT/30 electromechanical testing machine equipped with a 30 kN load cell, except for (1) compression specimens with 0° and 25° load-grain angle that were tested in INOVA - EDYZ 6 with 50 kN load cell and Inova ACS2500-100 with a 2500 kN load cell, respectively and (2) single edge notched arches that were examined in both INOVA - EDYZ 6 with 50 kN load cell and INOVA - Savad with $50 - 100$ kN load cell. Some samples were equipped with MTS-634.11F axial extensometer. Force, crosshead displacement and, if applicable, displacement from the extensometer were recorded at 10 Hz. For some tests, image data were collected for a subsequent digital image correlation (DIC) analysis. In these cases, a random pattern was sprayed on the monitored surfaces of the specimens before testing. During the test, the surface was photographed at regular intervals using Canon EOS 70D 20 megapixel digital camera fitted with Canon EF 100 mm $f/2.8$ lens. A particular attention was paid to synchronize the camera and data logger records so as to be able to link the photographs with the applied load. The DIC analyses were performed using the Ncorr v. 1.2 open-source software [75] with the Ncorr_post in-house graphical interface [76]. Taking into account the inhomogeneous character of wood, the strain from DIC was not evaluated locally but as the overall (spatially averaged) value over an area covering a representative domain of the sample. As an example, the representative region used for the off-axis samples is shown in Fig. 4.1a.

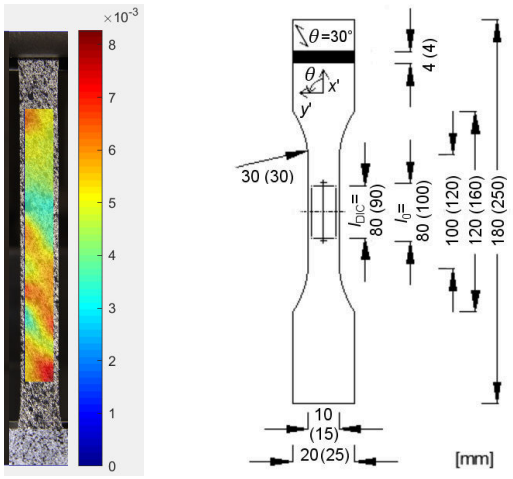

(a) (b)

Figure 4.1: Off-axis tension test: (a) strain in x' direction obtained by DIC for a specimen from group OT-30°, (b) dimensions for groups OT-4° to OT-90° with OT-0° and OT-1° (in brackets): gauge length l_0 and length of DIC area l_{DIC}.

Specimens group	OT-0°	OT-1°	OT-4°	OT-6°	OT-8°
Actual range of θ	$[0°, 1°)$	$[1°, 2°]$	$(2°, 5°]$	$(5°, 8°)$	$[8°, 10°]$
Specimens group	OT-20°	OT-30°	OT-50°	OT-90°	
Actual range of θ	$[18°, 23°]$	$[28°, 32°]$	$[45°, 53°]$	$[87°, 92°]$	

Table 4.1: Off-axis tension test groups.

4.3 Off-axis tension test

The off-axis tension test consists in applying uniaxial tension to specimens cut at different angles with respect to the grain. The test makes it possible to evaluate the elastic and strength parameters for two directions of orthotropy, parallel and perpendicular to the grain.

Dog bone shaped specimens complying with EN 408:1995 [19] and following the geometrical specifications of ISO 527 [77] in terms of dimensions were used. As, due to the inherent irregularity of wood structure, the real fiber orientation deviates from the intended one by units of degrees, we labeled the specimen groups prepared for testing using their real average load-grain angle θ rounded down to the nearest whole number, see Table 4.1. The specimens from groups OT-0° and OT-1° were cut from solid timber and those from groups OT-4° to OT-90° from 10.5 mm GLT. Dimensions are shown in Fig. 4.1b.

(a) (b) (c) (d) (e)

Figure 4.2: Examples of failure observed in the off-axis tensile test specimens: (a) OT-0°: splinter, (b) OT-0°: tension and shear, (c) OT-4°, (d) OT-50°, and (e) OT-90°.

The specimens were fitted with extensometer with gauge length of $l_0 =$ 80 mm except the OT-0° and OT-1°, for which l_0 was 100 mm. They were fixed to the loading machine using grips; the lower attachment was rigid, while the upper one allowed rotation about axis perpendicular to the specimen plane. Tests were conducted under displacement control with the displacement rate of 30 mm/s. In addition to recording the applied force P, crosshead displacement and extensometer readings, photographs for DIC analysis were taken at 10 sec intervals.

Out of the total of 122 tested specimens, 79% failed in the dog bone neck and only these results are discussed hereafter. Fig. 2.2 depicts the common types of timber failure encountered in tensile tests. Among the samples of the OT-0° and OT-1° groups, the failure in splinter (Fig. 4.2a) prevailed (78%) over the failure in tension-shear (Fig. 4.2b). For the groups OT-4° - OT-90°, we observed exclusively cracking parallel to the grain, see Fig. 4.2c - Fig. 4.2e. It should be also noted that there was no case when failure occurred along the glued interface between laminas, which means that the measured strengths correspond to those of the wood mass.

Fig. 4.3 shows the axial load-displacement curves obtained from the tests with different off-axis angles as recorded from the extensometer for OT-0° group or DIC images for OT-1° (Fig. 4.3a), OT-50°, and OT-90° groups (Fig. 4.3b). It is seen that the response is nearly linear up to failure. Since, in spite of controlling the test by displacement, the post-failure branch could not be captured, we were able to identify only the elastic and strength parameters from the results, as discussed in Sections 5.1 and 5.2.

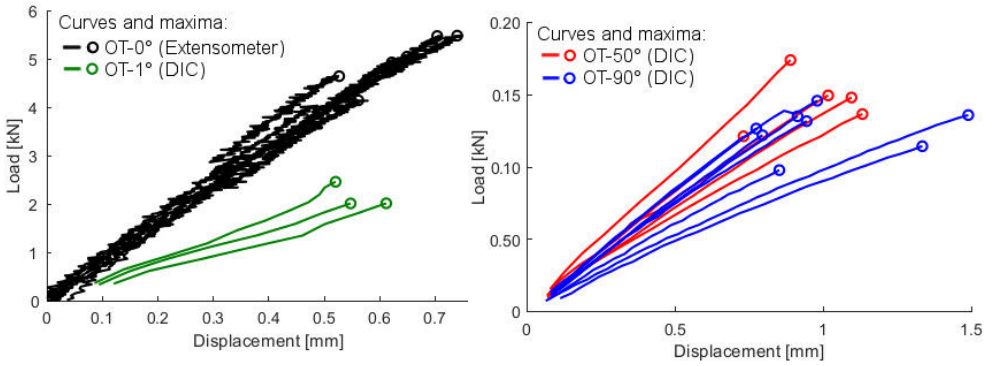

(a) (b)

Figure 4.3: Off-axis tension test results: load vs. displacement from extensometer or DIC analysis: (a) OT-0° and OT-1°, (b) OT-50° and OT-90°.

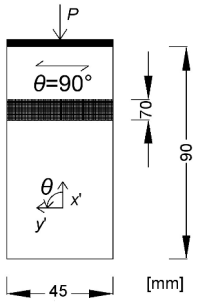

Figure 4.4: The off-axis compression test: specimen dimensions.

4.4 Off-axis compression test

Off-axis compression tests are analogous to the tensile tests in terms of the induced stress state and the parameters that they provide. However, to avoid global buckling, they are performed on block specimens as opposed to slender dog bones. To cut the specimens with the same size for the off-axis angles θ of 0°, 20°, 45°, and 90° (batches OC-0°, OC-20°, OC-45°, and OC-90°) from 10.5 mm GLT arches so as they fit into the arches' shape, we used the dimensions of 45 mm x 90 mm x 70 mm (Fig. 4.4), despite being specified by EN 408 [19] for the compression test of a solid timber with the load-grain angle of 90°.

At the beginning of the test, the specimen was placed centered on the steel platens of the loading machine. The lower platen was rigid while the upper one was hinged. No specific capping was applied on either side. Two extensometers with gauge length of 25 mm for the OC-0° group and

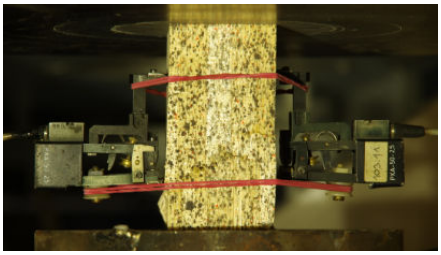

Figure 4.5: The off-axis compression test: test set-up.

(a) (b) (c) (d)

Figure 4.6: Off-axis compression test: failure in the mode of wedge splitting for off-axis angle 0° (a, b) and compression and shearing parallel to the grain for off-axis angle 20° (c, d). Figures (a, c) show the face view and figures (b, d) the side view of the specimen.

50 mm for the other groups were mounted on the specimens' sides (Fig. 4.5). Displacement-controlled loading was applied at the rate of 0.6 mm/min. The applied force P, crosshead displacement and extensometers' readings were recorded during the tests. Pictures for DIC analysis were taken with 5 sec time interval. The DIC data were used to evaluate strains in the same way as explained in Sections 4.2 and 5.1.

Specimens from the batch OC-0° typically fail under compression in one of the six modes depicted in Fig. 2.3. Out of them, the specimens with one of the last three modes (i.e. splitting, compression and shearing together with brooming or end-rolling) are to be culled according to the ASTM standard D143-94 [3]. From the total of 21 tested samples of OC-0° - OC-90° groups, 19 provided usable data. In group OC-0°, the most common failure was the wedge split (83%), see a specimen's face and side in Fig. 4.6a and Fig. 4.6b, respectively. The specimens from groups OC-20° and OC-45° failed in compression and shearing parallel to the grain as captured in Fig. 4.6c - Fig. 4.6d and Fig. 4.7a - Fig. 4.7b, respectively. The failure of samples belonging to group OC-90° was ductile with plastic deformations, see Fig. 4.7c and Fig. 4.7d.

(a) (b) (c) (d)

Figure 4.7: Off-axis compression test: failure in the mode of compression and shearing parallel to the grain for off-axis angle 45° (a, b) and ductile failure for 90° (c,d). Figures (a, c) show the face view and figures (b, d) the side view of the specimens.

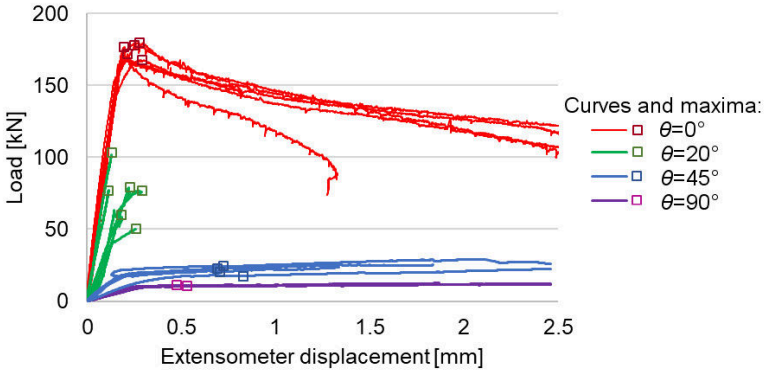

Figure 4.8: Off-axis compression test results: load vs. crosshead displacement for different load-grain angles θ.

Fig. 4.8 shows the measured load-displacement curves. It is seen that for OC-0° specimens, the response is initially almost linear, followed by some hardening and subsequently by a pronounced softening branch. The softening is associated with a progressive ingress of the wedge and splitting of the test prism (Fig. 4.6a and Fig. 4.6b). For OC-90° specimens, the initial linear part turns into a nearly perfectly plastic response characteristic for the development of dispersed plastic deformation. Similar overall load-displacement trend is observed also for OC-45°. However, in this case, this response can be attributed to sliding of the fragments (Fig. 4.7a and Fig. 4.7b) at high normal compression (from Eq. (5.2), $\sigma_y = -\tau_{xy} = 0.5\sigma_{x'}$), along the shear crack, which developed along the grain. For OC-20° specimens, the disintegration also occurs along the grain. However, this time, the relative sliding of the fragments is constrained, since the failure plane intersects with one of the loading plates (see Fig. 4.6c), which may contribute to the failure occurring at much higher load than in the case of OC-45° specimens (when the

failure surface passed through the free sides of the specimen). The response curves for the OC-20° group do not show any perfect-plastic part. Instead, the post-peak behavior was so brittle that it could not be captured. The compressive tests were used to evaluate only the elastic moduli and strengths, see Sections 5.1 and 5.2.

4.5 Shear test

As we discuss in Chapter 5, results of the off-axis tests for variable angles can be used to identify the shear strengths parallel to the grain for different combinations of shear and normal tension or compression. However, a more common method for determination of the pure shear strength is specified in the ASTM D143-94 standard [3]. Therefore, we included testing according to this specification in our campaign.

The specimen was a notched block made of 10.5 mm GLT with dimensions and configuration depicted in Fig. 4.9. Only specimens with fibers aligned with the loading direction were used. The specimens were freely laid on the steel base plate without capping or gluing. No extensometer was attached and the displacements were acquired from DIC measurements, with snapshots taken every 5 sec. The load was applied while controlling the crosshead displacement at a rate of 0.6 mm/min.

The specimens should fail by shearing-off in the direction parallel to the grain along the plane defined by the inner edge of the base plate and the inner corner of the notch. However, due to inherent imperfections of the material, in some specimens the fracture plane extended back onto the supporting surface. These results were ignored, as this failure is governed by the compressive resistance of the diagonal strut formed between the load and support plates, rather than by shear.

The specimens failed with the crack parallel to the grain more or less along the expected shearing area. The crack of the specimen S1 was slightly skewed heading from the inner edge of the notch towards the inner edge of the bottom support, see Fig. 4.10a. Compared to it, the cracks of the specimens S2-S4 were almost aligned with the specimens' longer edges spreading from the inner edge of the notch, see Fig. 4.10b. [17]

Fig. 4.11 shows the valid curves of load vs. relative vertical displacement $\Delta_{x,DIC}$. The latter was acquired from DIC measurements as depicted in

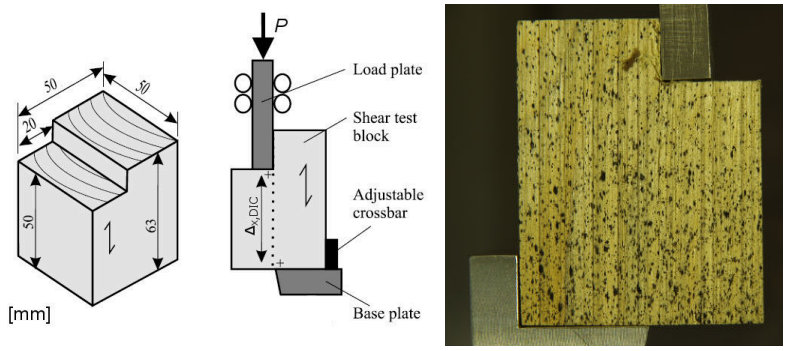

(a) (b)

Figure 4.9: Shear-parallel-to-grain test according to the standard ASTM D143-94: (a) set-up and virtual gauge over which the relative vertical displacement $\Delta_{x,DIC}$ was calculated by DIC analysis, (b) a mounted specimen.

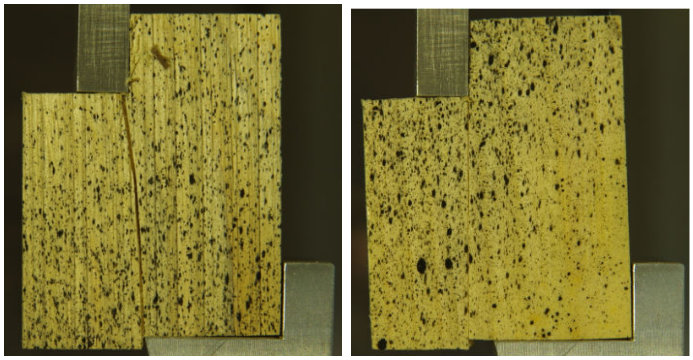

(a) (b)

Figure 4.10: The final fracture of the shear-parallel-to-grain test according to the standard ASTM D143-94: (a) the specimen S1 and (b) the specimen S3. [17]

Fig. 4.9a. It is seen that the peak values of force can be clearly identified. They are followed by a sudden drop, which was associated with an unstable fracture propagation. Therefore, the post-failure cohesive behavior could not be retrieved from the test.

4.6 Compact tension test

We should note that none of the previous test configurations allowed us to capture the post-failure response under shear and/or tension and, thus, to determine the fracture energy or traction-separation relation. To obtain the fracture properties in the crack-normal direction for the crack parallel to the grain, we used the compact tension test with the load-grain angle $\theta = 90°$

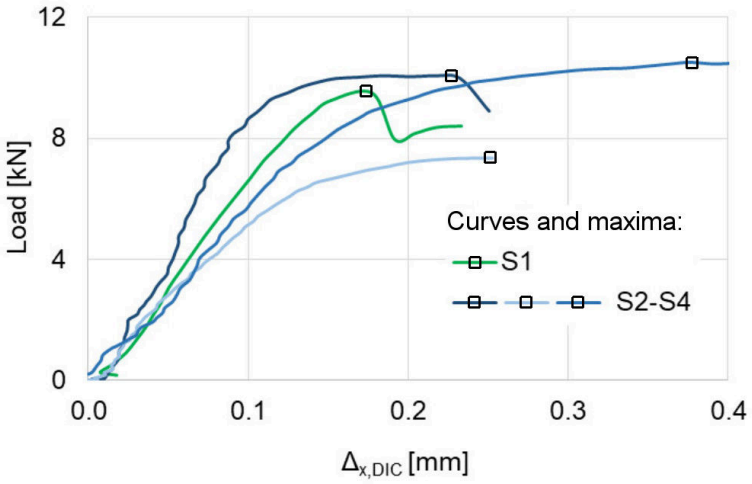

Figure 4.11: Results of the shear-parallel-to-grain test according to the norm ASTM D143-94 standard [3]: load vs. DIC relative vertical displacement $\Delta_{x,DIC}$ (from DIC). The maximum load is marked with square.

according to the ASTM E1820-09 standard [78] (group CT-90°). We cut the specimens from 45 mm GLT. The specimens were fitted with extensometer with gauge length of $l_0 = 12$ mm placed at the notch mouth, see Fig. 4.12a.

With the aim of obtaining the fracture behavior in the crack-normal direction governed by the fiber rupture, we used the CT specimens with the load-grain angle $\theta = 0°$ (group CTC-0°). The specimen size and general test arrangement was the same as for group CT-90°. Furthermore, to encourage crack propagation perpendicular to the grain, the test configuration was modified by (1) pre-straining the specimens to approx. $\varepsilon_{y'} = \{0.0074, 0.0090\}$ mm/mm in the direction perpendicular to the loading, which corresponded to pre-stress $\Delta\sigma_{y'}$ of about 2.7 to 3.3 MPa (Fig. 4.12b), and (2) reducing the ligament depth to 10 mm (Fig. 4.12c).

For both groups CTC-0° and CT-90°, the load was applied under crosshead displacement control at a rate of 0.5 mm/min. Photos for the DIC analysis were taken at 5 sec time interval.

All sixteen CT specimens of group CT-90° failed with the failure type that we denote as F0 - disintegration parallel to the grain initiated at or around the notch tip. In this case, the crack spread along the ligament. In group CTC-0°, two specimens out of five failed with the failure type F0 with the crack propagating perpendicular to the ligament, see an example in Fig. 4.13a. In one of them the failure type F0 was followed by shearing inside the timber lamina, see an example in Fig. 4.13b. The failure type that we denote as F1,

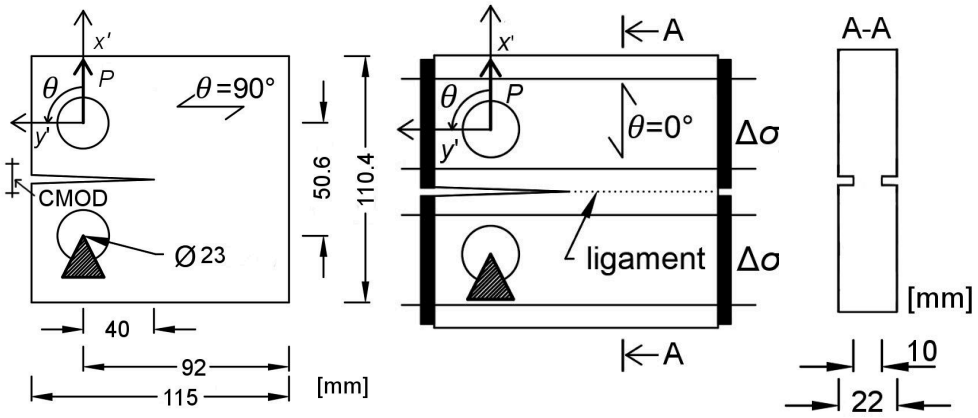

(a) (b) (c)

Figure 4.12: Compact tension test configuration and dimensions. (a) Group CT-90°, front view. (b) Group CTC-0°, front view. (c) Group CTC-0°, side view.

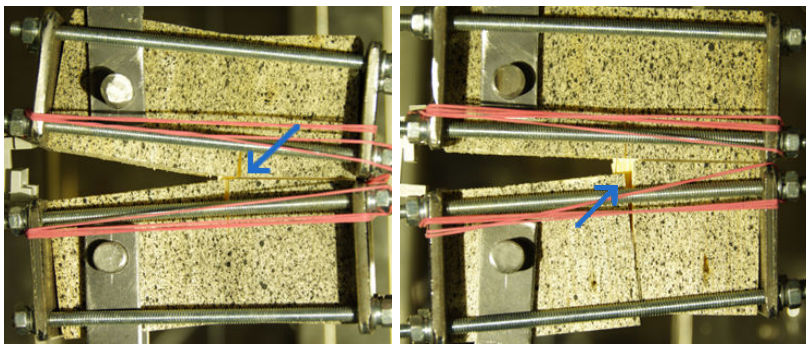

(a) (b)

Figure 4.13: Failure of pre-stressed CTC-0° specimens: (a) type F0 and (b) type F0 followed by shearing-off.

in which fibers' rupture is concentrated around or at the cross-section ahead of the notch (Fig. 4.14a), occurred once. In two specimens out of five, failure type F2 with fibers' rupture concentrated around or at the cross-section ahead of the notch accompanied by disintegration parallel to the grain was observed. The disintegration propagated either from the cross-section's middle, denoted as F2-a (Fig. 4.14b), or from both the notch tip and the cross-section's third, denoted as F2-b, (Fig. 4.14c).

The obtained responses are shown for the group CT-90° and CTC-0° in Fig. 4.15a and Fig. 4.15b, respectively. All sixteen CT-90° response curves exhibited linear behavior followed by softening. It reflects, that only the failure type F0 with the crack propagating along the ligament occurred. Compared to it, the CTC-0° responses differed both in response features and failure types. The first part of all five curves exhibit linear behavior. Then,

(a) (b) (c)

Figure 4.14: Failure of pre-stressed CTC-0° specimens: (a) type F1, (b) type F2-a, and (c) F2-b.

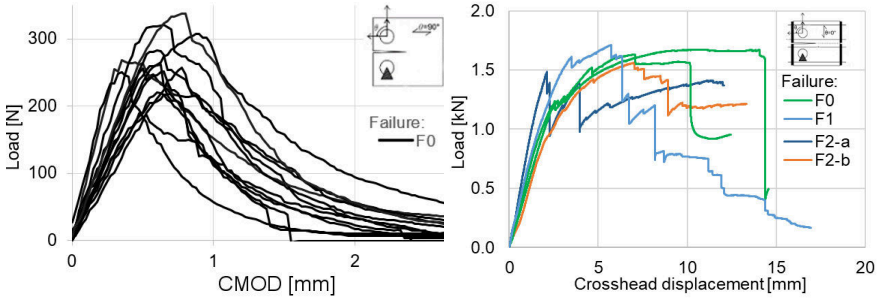

(a) (b)

Figure 4.15: (a) Load vs. crack-mouth opening displacement (CMOD) for the specimens of group CT-90°, which all failed in mode F0, and (b) load vs. crosshead displacement for pre-stressed CT specimens of group CTC-0° that failed in modes F0, F1, and F2.

in two specimens with failure type F0, it is followed by hardening, as the crack perpendicular to the ligament developed, and a drop representing the shearing or shearing-off. In the specimen with failure type F1, the linear part proceeded with a softening branch composed of little drops, as fibers' bundles ruptured, alternating with hardening portions, as the bundles disintegrated around or at the cross-section ahead of the notch. In the specimen with failure type F2-a, the linear response was followed by softening and hardening portions due to fibers' rupture along the ligament up to its middle where disintegration started to propagate perpendicularly. In the specimen with failure type F2-b, the linear response was followed by (1) a decrease in slope, as disintegration propagated from the notch tip, (2) softening portion related to fibers' rupture developed up to the ligament's third, and (3) hardening during which disintegration started to propagate perpendicularly from the ligament's third.

In summary, the tests CT-90° provided consistent load-CMOD data, which characterize the crack growth in mode-I parallel to the grain up to the complete separation and can be used to identify corresponding traction-separation relation and fracture energy, as discussed in Chapter 5. On the other hand, the tests CTC-0° should be interpreted only qualitatively for the following reasons:

- Since the lateral preloading was applied as prescribed strain, the actual prestress was only estimated using Young modulus and may not be accurate.
- During the failure type F0, cracks were propagating along the grain in mixed mode I and II. Failure occurred at large crosshead displacements and involved extensive compressive damage on the outer side of the ligament opposite to the notch. The obtained load-displacement data are contaminated by the geometrical non-linearity as well as compressive material non-linearity and thus cannot be used to characterize the crack growth parallel to the grain.
- In only one case the failure could be clearly linked to the rupture of fibers bridging the ligament (failure type F1). Therefore, the test does not provide enough data to evaluate the corresponding fracture energy and traction-separation law with sufficient confidence.
- Recent works [79, 80] show that in quasi-brittle materials, such as concrete, mode-I fracture energy is strongly affected by the crack-parallel normal stress. We assume that fracture perpendicular to the grain in wood may also exhibit this effect since the fracture process zone is tortuous and involves pullout of ruptured fiber bundles, which may be constrained by the lateral compression. This phenomenon deserves further systematic investigation.

4.7 Three-point bending test on notched beams

Within the author's previous work [18], an attempt to retrieve the post-failure behavior from small-size notched beams with fibers along the beam length under three-point bending was made. Since these tests provide a complementary insight on the timber fracture behavior, we briefly summarize them below.

Two groups of prismatic notched beams (Fig. 4.16) were prepared. All beams shared the same length (400 mm), height (100 mm), and the notch

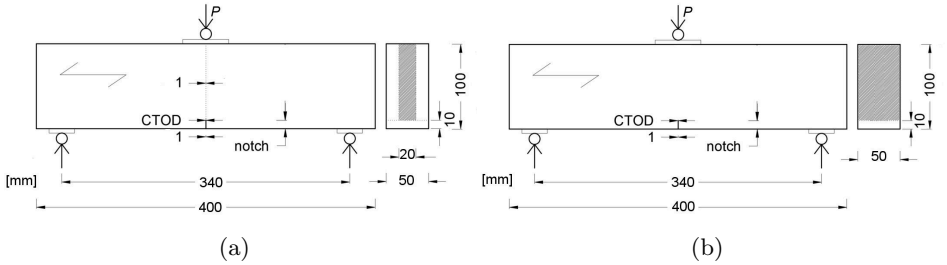

Figure 4.16: Configuration of the three-point bending tests on notched beams: (a) group 3PB-A with reduced cross-sectional area above notch, (b) group 3PB-B without reduction.

depth of 10 mm and width of 1 mm. The first group (3PB-A) collected beams with the thickness of 50 mm. The cross-sectional area above the notch was further reduced by two 15 mm deep and 1 mm wide slits sawn symmetrically from the front and back side of the specimen. Group 3PB-A included 8 specimens cut from solid timber (spec. $\#1 - \#8$) and 2 specimens made of 45 mm GLT (spec. #9, #10). The second group (3PB-B) was manufactured with a uniform thickness of 40 mm and no reduction of the cross-section above the notch. It consisted of 4 samples (spec. $\#11 - \#14$) made of 45 mm GLT. During testing, the beams were supported by 50 mm wide steel plates placed on rollers. The same arrangement was also used to apply the load (Fig. 4.16). We ran the tests under displacement control at a rate of 2 mm/min.

The beams from the group 3PB-A with the reduced cross-section failed with the failure type that we denote as F1 - fibers' rupture concentrated around or at the cross-section ahead of the notch or type F2 - fibers' rupture around or at the cross-section ahead of the notch accompanied by disintegration propagating along the grain. The response and fracture of the beams with the failure type F1 is shown in Fig. 4.17 and the failure type F2 in Fig. 4.18. The disintegration within the failure type F2 involved either (1) shearing-off along a nearly horizontal surface passing through the full thickness of the beam (e.g. spec. #8 in Fig. 4.18b) or (2) pullout of a fiber bundle (e.g. spec #9 in Fig. 4.18b). It should be noted that the solid timber samples exhibited both types of failure F1 and F2, while only type F2 was seen in the GLT samples. However, even in the GLT the shearing-off occurred in the timber mass and not in the glued interlaminar interface.

The beams from the group 3PB-B with no reduction of the cross-sectional area above the notch failed in mode F3 – multiple disintegration parallel to the grain. Splitting cracks initiated at the notch tip and propagated along the grain. Under further loading, fibers' rupture took place above the notch and additional splitting/shear cracks developed. The recorded response of the beams is shown in Fig. 4.19 together with the final crack pattern detail of the specimen #14. Summary of the experimental results is presented in

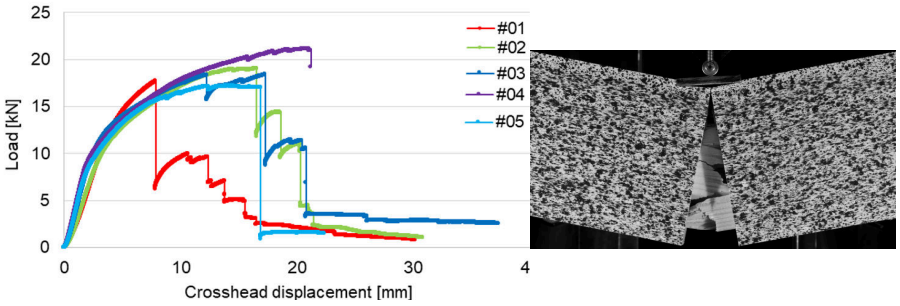

(a) (b)

Figure 4.17: (a) Load vs. crosshead displacement for the beams of the group 3PB-A failing in mode F1. (b) Fracture of the beam #2. [18]

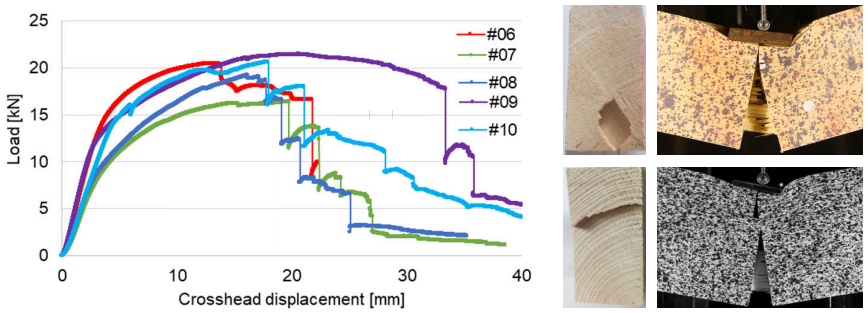

(a) (b)

Figure 4.18: (a) Load vs. crosshead displacement for the beams of group 3PB-A failing in mode F2. (b) Fracture of the beam #09 with pullout of a bundle (upper) and beam #08 with throughout shear-off surface (lower). [18]

Table 4.2.

As seen in Fig. 4.17 and Fig. 4.18, the responses of the beams with the failure type F1 and F2 are similar in terms of the peak forces and corresponding displacements. They, however, differ in the trend of the descending branches, which is steeper for the beams with failure type F1. This can be attributed to the fact, that in the case of F1, the material damage is concentrated to a smaller volume resulting in less energy dissipation. As indicated in Fig. 4.19, the specimens failing in mode F3 show a more pronounced hardening before the peak, which can be associated to the development of multiple cracks prior to collapse.

Similarities in failure type can be found comparing the 3PB test on notched beams with the CT test on pre-stressed CTC-0° specimens. The failure type F1 occurred in 5 out of 10 specimens in group 3PB-A and in 1 out of 5 specimens in group CTC-0°. The failure type F2 was observed in 5 out of 10 specimens in group 3PB-A and 2 out of 5 specimens CTC-0° group. The failure type F0, that is also the first cracking of the F3 failure (multiple

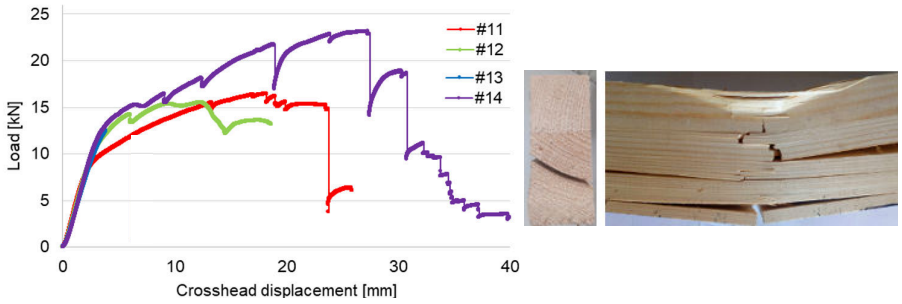

(a) (b)

Figure 4.19: (a) Load vs. crosshead displacement for the beams of the group 3PB-B with the first failure F3 - parallel to the grain. (b) Failure detail for the beam #14 with throughout shear-off surface. [18]

Group	Material	N [–]	Failure type	Specimens
	Solid	5	F1	#01 - #05
3PB-A	Solid	3	F2	#06 - #08
	45 mm GLT	2	F2	#09 - #10
3PB-B	45 mm GLT	4	F3	#11 - #14

Table 4.2: Summary of the three-point bending tests on notched beams. (Transcribed from [18].)

disintegration parallel to the grain), was present in all 4 specimens of the 3PB-B group and in 2 out of 5 CTC-0° specimens. We can see that the fibers' rupture accompanied or not by disintegration (failure types F1 and F2) was present in 3 out of 5 CTC-0° specimens, which is less frequent than in 3PB-A specimens, where it occurred in all 10 specimens. Multiple or not, the disintegration parallel to the grain (failure type F3 and F0) was observed in 2 out of 5 CTC-0° specimens, which is less frequent than in 3PB-B specimens, in which it occurred in all 4 specimens.

It should be noted that extensive compressive plastic deformations near the loading and support plates and, in some cases, inter-grain damage extending far away from the fracture plane above the notch was observed in the tests. Therefore, the obtained load-displacement curves were deemed not suitable for a quantitative evaluation of the fracture energy or traction-separation relationship and we limit ourselves to only qualitative comparison of the load-displacement behavior.

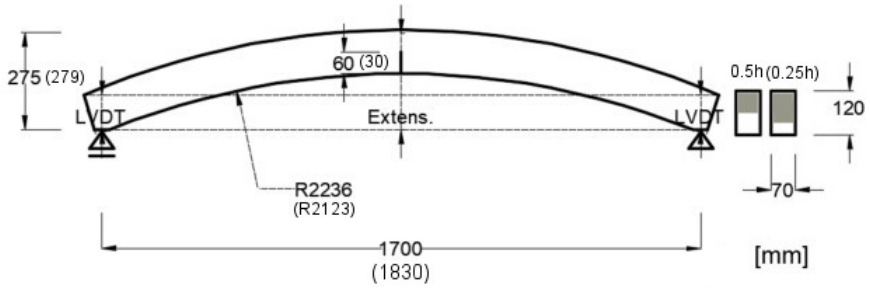

Figure 4.20: Dimensions of the arch with the $0.5h$ ($0.25h$) notch.

4.8 Three-point bending test on notched arches

Unlike the material experiments primarily designated for the calibration of the proposed model, which are depicted in the Sections 4.3 - 4.7 above, the three-point bending test on notched arches was intended for the model validation. The test configuration was designed so as the cracks propagated under tensile-shear stress states.

We prepared two sets of arches with four and three specimens made of European spruce glued laminated timber with the lamina thickness of 10.5 mm, hereinafter referred to as 10.5 mm GLT, and dimensions depicted in Fig. 4.20. Vertical notches, 1 mm wide, were saw-cut in the mid-span of the specimens. The notches extended to one half of the specimen height h for the series with 1700 mm span and one quarter of h for the series with 1830 mm span, hereinafter referred to as $0.5h$ and $0.25h$, respectively. The arches were simply supported and exposed to the three-point bending under displacement control at a constant rate of 2 mm/min. The load was applied through an 80 mm wide distribution plate made of steel. The arches' deflection was measured by LVDT 1 cm under the vertical axis of the loading plate. Two LVDTs were also placed above both supports aligned with their vertical axes, see Fig. 4.20 and Fig. 4.21. Digital images were captured at 5 sec time interval for a subsequent digital image correlation (DIC) analysis.

In arches with the notch of $0.5h$, hereinafter denoted as "exp_0.5h-1" to "exp_0.5h-4", the primary crack initiated at the notch tip and propagated parallel to the grain, see Fig. 4.22a. Furthermore, in the specimens "exp_0.5h-1" and "exp_0.5h-4", we also observed a secondary crack parallel or oblique to the arch longitudinal direction that branched from the primary one in the area above the notch, see Fig. 4.22b. The development of both crack patterns is presented for the deflection of 10 mm, 25 mm, 40 mm, and 45 mm. The Fig. 4.23 shows the measured responses of the arches from the experiments

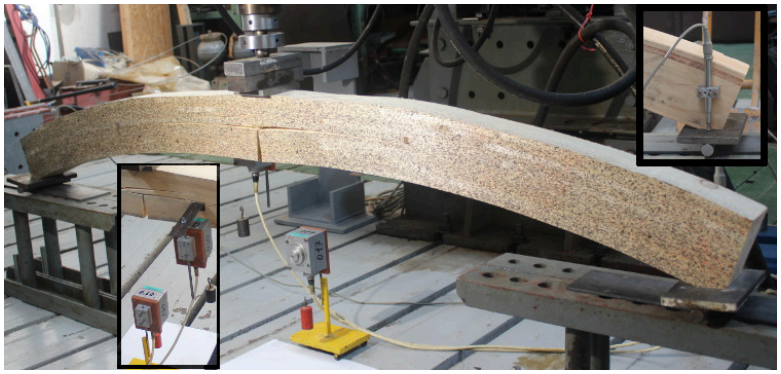

Figure 4.21: Arch test setup. Left and right detail with deflection and LVDT measurement, respectively.

in terms of the load and mid-span deflection. Comparing these responses and the respective crack patterns in the photos taken for DIC, we can see, that the drops in the load for "exp_0.5h-1" and "exp_0.5h-4" arches at $35-40$ mm deflection represent the secondary crack initiation.

In arches with the notch of $0.25h$, hereinafter denoted as "exp_0.25h-1" to "exp_0.25h-3", the primary crack initiated at the notch tip from where it grew only a little in the direction parallel or slightly oblique to the arch longitudinal direction. In the specimen "exp_0.25h-2", the primary crack propagated parallel to the specimen longitudinal direction, and consequently, a secondary crack parallel to the grain occurred at mid-height. Compared to it, in specimens "exp_0.25h-1" and "exp_0.25h-3", the primary crack propagated from the notch tip upwards obliquely to the arch shape, up to the fiber layer at mid-height, where a secondary crack started to grow parallel to the grain. The crack development in the arch "exp_0.25h-2" and "exp_0.25h-3" is shown in Fig. 4.24a and Fig. 4.24b, respectively, at the deflection of 10 mm, 20 mm, and 45 mm. Comparing the responses shown in Fig. 4.23 and images recorded for DIC, we can see that the significant decrease in load is connected to the crack initiation in another fiber layer.

4.9 Partial summary

This chapter presents an experimental study containing off-axis tension and compression tests, shear block tests, compact tension tests, and three-point bending tests of single edge notched beams and arches. As the tension, compression, shear, and compact tension specimens were cut with a typical size on the order of 10^{-2} m, the reported data should be considered as

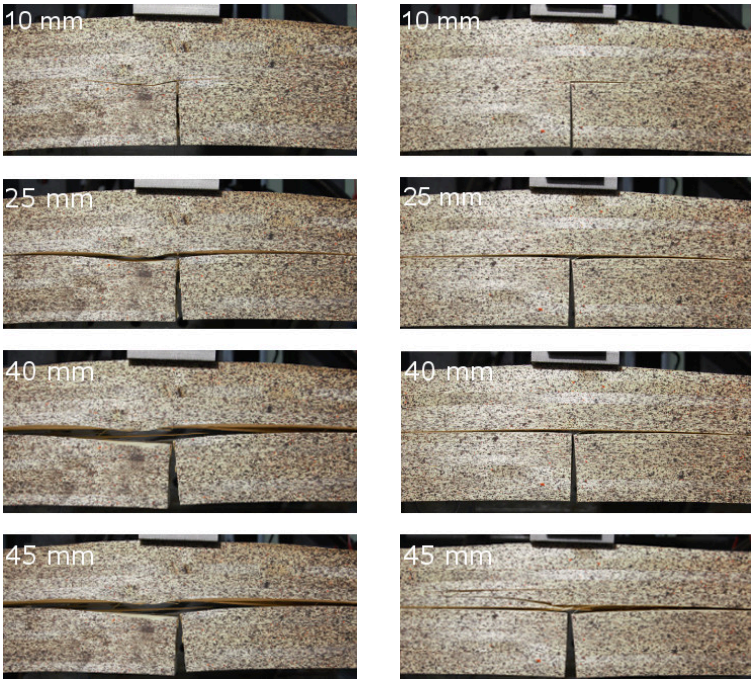

(a) (b)

Figure 4.22: Crack development in the arches (a) "exp_0.5h-2" and (b) "exp_0.5h-1" (from the top) at 10 mm, 25 mm, 40 mm, and 45 mm deflection.

representing properties of a clear wood or GLT material, and not as those of the whole timber structural members. Compared to it, the results from the tests of the beams and arches may be adversely affected by the presence of flaws, such as knots, shakes, etc. As these flaws were observed outside of the fracture zone, the test result were only negligibly influenced by them. Thus, they were neglected in the simulations presented in Chapters 6 and 7. If these defects are to be taken into account, they should be adequately represented in the finite element model.

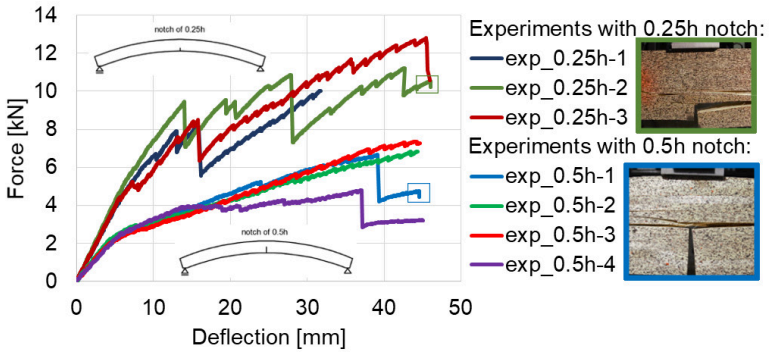

Figure 4.23: Experimentally obtained load-deflection curves for the arches with the vertical notch of $0.25h$ and $0.5h$ with a detail of cracking for "exp_0.25h-2" and "exp_0.5h-1" at 45 mm deflection.

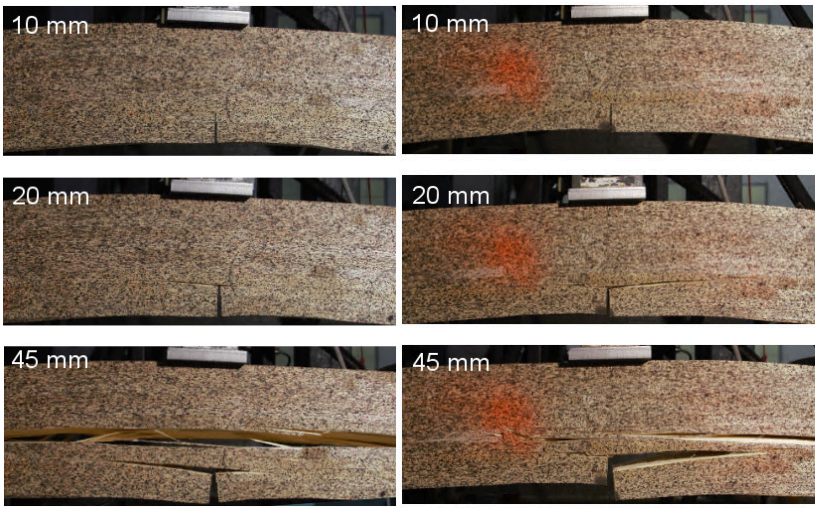

(a) (b)

Figure 4.24: Crack development in the arches (a) "exp_0.25h-2" and (b) "exp_0.25h-3" (from the top) at 10 mm, 20 mm, and 45 mm deflection.

Chapter 5

Calibration of the constitutive model

This chapter describes methodology adopted for the evaluation of the test results and the consequent calibration of the proposed model. The text is taken from [35].

5.1 Elastic moduli and Poisson's ratios

The results of the off-axis tension tests (Section 4.3) were used to determine the elastic parameters (moduli and Poisson's ratios). To this end, the difference of load and displacement or strain over the linear part of the load-displacement curve between 10% and 40% of the peak load was considered.

To quantitatively interpret the results, we have to consider the 2D stress and strain state, which arise in the off-axis tension test, as shown in Fig. 5.1. Here the prime '′' denotes the global coordinate system. The axis x' is co-linear with the direction of the load P that is applied axially with the tensile specimen and y' is perpendicular to it. The axis x has the same direction as fibers and y is perpendicular to it. The applied force P produces stress $\boldsymbol{\sigma}'$ referenced to the $x' - y'$ system of coordinates:

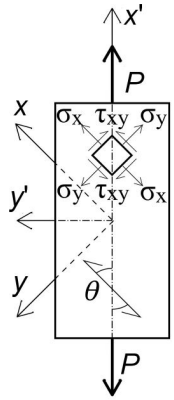

Figure 5.1: 2D stress state [15].

$$\boldsymbol{\sigma}' = \begin{Bmatrix} \sigma_{x'} \\ \sigma_{y'} \\ \tau_{x'y'} \end{Bmatrix} = \begin{Bmatrix} \frac{P}{A} \\ 0 \\ 0 \end{Bmatrix} \tag{5.1}$$

where A is the area of the specimen neck cross-section perpendicular to the loading direction x'. Actual size of this area was calculated using the measured dimensions of each specimen. Due to the material orthotropy, the corresponding strain $\boldsymbol{\varepsilon}' = \{\varepsilon_{x'}, \varepsilon_{y'}, \gamma_{x'y'}\}^T$ may generally have all three components non-zero. Stress and strain vectors can be transformed to the material coordinate system $x-y$ by pre-multiplying them with the appropriate transformation matrix:

$$\boldsymbol{\sigma} = \begin{Bmatrix} \sigma_x \\ \sigma_y \\ \tau_{xy} \end{Bmatrix} = \begin{bmatrix} \cos^2\theta & \sin^2\theta & 2\sin\theta\cos\theta \\ \sin^2\theta & \cos^2\theta & -2\sin\theta\cos\theta \\ -\sin\theta\cos\theta & \sin\theta\cos\theta & \cos^2\theta - \sin^2\theta \end{bmatrix} \begin{Bmatrix} \sigma_{x'} \\ \sigma_{y'} \\ \tau_{x'y'} \end{Bmatrix} = \boldsymbol{T}_\sigma \boldsymbol{\sigma}' \tag{5.2}$$

$$\boldsymbol{\varepsilon} = \begin{Bmatrix} \varepsilon_x \\ \varepsilon_y \\ \gamma_{xy} \end{Bmatrix} = \begin{bmatrix} \cos^2\theta & \sin^2\theta & \sin\theta\cos\theta \\ \sin^2\theta & \cos^2\theta & -\sin\theta\cos\theta \\ -2\sin\theta\cos\theta & 2\sin\theta\cos\theta & \cos^2\theta - \sin^2\theta \end{bmatrix} \begin{Bmatrix} \varepsilon_{x'} \\ \varepsilon_{y'} \\ \gamma_{x'y'} \end{Bmatrix} = \boldsymbol{T}_\varepsilon \boldsymbol{\varepsilon}' \tag{5.3}$$

The stress and strain vectors in the material coordinate system are then related by the orthotropic elastic constitutive law for plane stress:

$$\boldsymbol{\varepsilon} = \begin{bmatrix} \frac{1}{E_x} & \frac{-\nu_{yx}}{E_y} & 0 \\ \frac{-\nu_{xy}}{E_x} & \frac{1}{E_y} & 0 \\ 0 & 0 & \frac{1}{G_{xy}} \end{bmatrix} \boldsymbol{\sigma} = \begin{bmatrix} C_{11} & C_{12} & 0 \\ C_{21} & C_{22} & 0 \\ 0 & 0 & C_{33} \end{bmatrix} \boldsymbol{\sigma} = \boldsymbol{C}\boldsymbol{\sigma} \tag{5.4}$$

where E_x, E_y are Young's moduli, G_{xy} is the shear modulus, ν_{xy}, ν_{yx} are Poisson's ratios, and $\boldsymbol{C}$ is compliance matrix with elements $C_{11} - C_{33}$. Due to the symmetry, the following relation must hold:

$$\frac{-\nu_{xy}}{E_x} = \frac{-\nu_{yx}}{E_y} \tag{5.5}$$

First, the specimens OT-0° and OT-90° were used to obtain the elastic moduli and tensile strengths in directions parallel (E_x, f_x) and perpendicular (E_y, f_y) to the grain, respectively. For the calculation we used Eq. (5.1) - Eq. (5.4). For OT-0° group, the axial strain $\varepsilon_{x'} = \varepsilon_x$ for calculation of E_x was determined by dividing the extensometer displacement readings $u_{x'}$ with the gauge length l_0. Increments of load ΔP and deformation $\Delta u_{x'}$ were calculated by linear regression of the load vs. displacement curve within the interval of 10% – 40% of the maximum load:

$$E_x = \frac{\frac{\Delta P}{A}}{\frac{\Delta u_{x'}}{l_0}} \tag{5.6}$$

In addition, the transversal strain $\varepsilon_{y'} = \varepsilon_y$ evaluated from DIC was used to calculate Poison's ratio ν_{xy} from Eq. (5.4) as:

$$\nu_{xy} = -\frac{\varepsilon_y}{\varepsilon_x} \tag{5.7}$$

For OT-90° group, the axial strain $\varepsilon_{x'}$ for identification of E_y was determined by DIC analysis with spatial averaging over a representative domain depicted in Fig. 4.1b. The parameter E_y was calculated similarly as E_x for OT-0° in Eq. (5.6):

$$E_y = \frac{\frac{\Delta P}{A}}{\frac{\Delta u_{x'}}{l_0}} \tag{5.8}$$

The ratio ν_{yx} was then solved using Eq. (5.5). To find the shear modulus G_{xy}, first, we used transformation of compliance matrix $\boldsymbol{C}$ from the material coordinate system $x-y$ to the loading coordinate system $x'-y'$:

$$\boldsymbol{C}' = [\boldsymbol{T}_\varepsilon]^{-1}\boldsymbol{C}\boldsymbol{T}_\sigma \tag{5.9}$$

Then, we used Eq. (5.1) and the relation for the stress and strain vectors, $\boldsymbol{\sigma}'$ and $\boldsymbol{\varepsilon}'$:

$$\boldsymbol{\varepsilon}' = \begin{bmatrix} C'_{11} & C'_{12} & C'_{13} \\ C'_{21} & C'_{22} & C'_{23} \\ C'_{31} & C'_{32} & C'_{33} \end{bmatrix} \begin{Bmatrix} \frac{P}{A} \\ 0 \\ 0 \end{Bmatrix} = \boldsymbol{C}'\boldsymbol{\sigma}' \tag{5.10}$$

that yields set of three equations:

$$\begin{cases} \frac{\varepsilon_{x'}}{\sigma_{x'}} = (c^4\frac{1}{E_x} + s^4\frac{1}{E_y} - 2c^2s^2\frac{\nu_{yx}}{E_y} + c^2s^2\frac{1}{G_{xy}})\frac{1}{(c^2+s^2)^2}, \\ \frac{\varepsilon_{y'}}{\sigma_{x'}} = (c^2s^2\frac{1}{E_x} + c^2s^2\frac{1}{E_y} - (c^4+s^4)\frac{\nu_{yx}}{E_y} - c^2s^2\frac{1}{G_{xy}})\frac{1}{(c^2+s^2)^2}, \\ \frac{\gamma_{x'y'}}{\sigma_{x'}} = (cs(2c^2\frac{1}{E_x} - 2s^2\frac{1}{E_y} + 2(c^2-s^2)\frac{\nu_{yx}}{E_y} + (s^2-c^2)\frac{1}{G_{xy}}))\frac{1}{(c^2+s^2)^2}. \end{cases} \tag{5.11}$$

where c and s stand for $\cos\theta$ and $\sin\theta$. With all the remaining elastic constants being known, we used the results of OT-50° tests, including the axial strain $\varepsilon_{x'}$ obtained by DIC analysis, and Eq. (5.11) to calculate the shear modulus G_{xy}:

$$G_{xy} = \frac{-cs\sigma_{x'}}{(c^2-s^2)\gamma_{x'y'} + 2cs(\varepsilon_{y'} - \varepsilon_{x'})} \tag{5.12}$$

The results of the off-axis tensile tests are summarized in Table 5.1.

Even though in ideal elasticity the Young moduli in tension and compression should be the same, in general these constants obtained from the respective tests on timber may differ [81]. Therefore, we used the results of the tests described in Section 4.4 to evaluate Young moduli in compression. Following

Test	Angle θ [°]	Parameter	N [-]	Avg	CoV [-]
Tensile	0	E_x [MPa]	6	12418.0	0.04
Off-axis	0	f_x [MPa]	6	77.6	0.09
	90	E_y [MPa]	8	371.0	0.20
	90	f_y [MPa]	8	3.2	0.13
	0	ν_{xy} [-]	4	0.37	0.12
	0	ν_{yx} [-]	4	0.01	0.12
	50	G_{xy} [MPa]	5	310.0	0.23
	0 - 90	f_{xy} [MPa]	122	8.5	0.63
Compress.	0	E_{cx} [MPa]	3	16142.0	0.13
Off-axis	0	f_{cx} [MPa]	3	56.3	0.03
	90	E_{cy} [MPa]	6	310.0	0.19
	90	f_{cy} [MPa]	6	3.3	0.03
Shear	-	f_{xy}^{ASTM} [MPa]	4	3.7	0.16

Table 5.1: Elasticity and strength parameters evaluated from the off-axis tension and compression tests and the shear test for solid timber and 10.5 mm GLT. Symbol N is the number of valid test results used to calculate the mean Avg and the coefficient of variation CoV.

the same procedure as for the off-axis tension tests, the moduli were calculated from Eq. (5.6) and Eq. (5.8) for the difference of load and displacement over the linear part of the load-displacement curve between 10% and 40% of the maximum load P_{max}. The iterative calculation of P_{max} for compression test is described in Section 5.2.1.

We compared the calculated elastic parameters for European spruce from Table 5.1

$$\begin{aligned} E_x : E_y : G_{xy} &= 40.1 : 1.2 : 1, \\ E_{cx} : E_{cy} : G_{xy} &= 52.1 : 1 : 1, \\ \nu_{xy} : \nu_{yx} &= 37.0 : 1. \end{aligned} \tag{5.13}$$

with parameters for the same species from the literature [81]

$$\begin{aligned} E_x : E_y : G_{xy} &= 26.1 : 5.4 : 1, \\ E_{cx} : E_{cy} : G_{xy} &= 23.8 : 1.4 : 1, \\ \nu_{xy} : \nu_{yx} &= 17.5 : 1. \end{aligned} \tag{5.14}$$

where $G_{xy} = 573$ MPa and $\nu_{yx} = 0.028$. The values obtained in the present study fall in the ranges reported in the literature [38, 71, 82].

5.2 Failure criterion

As seen in Eq. (3.1) to Eq. (3.4), the failure surface is defined by five parameters: the uniaxial tensile and compressive strengths parallel and perpendicular to the grain (f_x, f_{cx}, f_y, f_{cy}, resp.) and the shear strength (f_{xy}).

5.2.1 Tensile and compressive strengths

The values of tensile and compressive strengths parallel and perpendicular to the grain can be directly retrieved from the tensile (groups OT-0° and OT-90°) and compressive tests (groups OC-0° and OC-90°). To this end, the maximum attained force P_{max} is divided by cross-sectional area A:

$$f = \frac{P_{max}}{A} \tag{5.15}$$

For the positive values of P_{max} applied in OT-0° and OT-90°, f takes the tensile strength values f_x and f_y. For the negative values of P_{max} applied in OC-0° and OC-90°, the compressive strength values f_{cx} and f_{cy} are adopted.

The value of P_{max} in compression test was evaluated iteratively in accordance with EN 408 standard [19] using the load-deformation curve, see Fig. 5.2. First, the value of P_{max}^{exp} was estimated. Then, a straight line going through two points, which were obtained as intersections of $0.1P_{max}^{exp}$ and

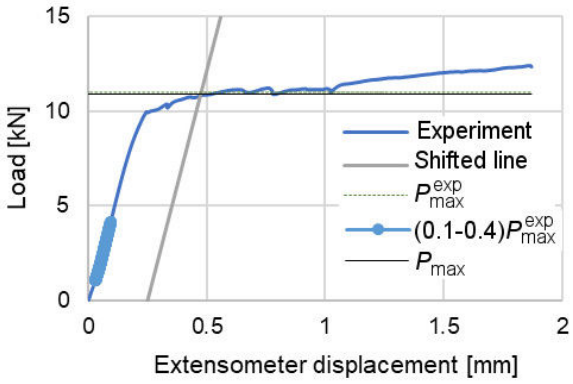

Figure 5.2: Iterative evaluation of P_{max} for compression test from OC-90° group according to EN 408 standard [19].

$0.4P_{max}^{exp}$ with the curve, was shifted by the distance of one hundredth of the gauge length ($0.01l_0$). Where the shifted line intersected the experimental curve was the P_{max}. If it was within 5% quantile of P_{max}^{exp} then the value was accepted, otherwise, the procedure was repeated until the tolerance was obtained.

Tensile and compressive strengths are listed in Table 5.1. We compared these calculated strength parameters:

$$f_x : f_y = 24.3 : 1, f_{cx} : f_{cy} = 17.1 : 1. \tag{5.16}$$

where f_y is almost the same as f_{cy}, with parameters for the same species from the literature [81]:

$$f_x : f_y = 33.8 : 1, f_{cx} : f_{cy} = 10.0 : 1. \tag{5.17}$$

where $f_y = 2.2$ MPa and $f_{cy} = 3.4$ MPa. The strength values obtained in the present study fall in the ranges reported in the literature [38, 71, 82].

5.2.2 Shear strength

As we discussed in Section 4.5, the ASTM D143-94 standard [3] specifies a methodology that is commonly used to determine the shear strength of timber. Using the maximum load P_{max} attained in the experiment, the shear strength f_{xy}^{ASTM} is calculated as:

$$f_{xy}^{ASTM} = \frac{P_{max}}{A} \tag{5.18}$$

where A is the shearing area. As seen in Fig. 4.9 the design shearing area was 2500 mm^2. Actual size of this area was calculated using the measured dimensions of each specimen [3]. The resulting strength is included in Table 5.1.

It was shown in a separate numerical study [17] that the surface along which fracture eventually develops in this test sustains nonuniform stressing with high stress concentrations near the loading and supporting blocks' edges before and after the specimen fails. Eq. (5.18) does not capture these peaks and estimates the strength as the average shear stress on the fracture area. This is acceptable and conservative if the test is used to evaluate capacity of a structural member whose critical section size is comparable with tested specimen. However, in finite element analyses, where the present data are to be used to calibrate the constitutive model, the resolution of stress field may be finer. Therefore, the ASTM test may not be appropriate to calibrate the parameters of the failure criterion and a more elaborate procedure, proposed below, has to be used.

The idea consists in utilizing results of the off-axis tension and compression tests, in which the surface, on which the crack eventually develops, is exposed to a nearly uniform stressing up to the specimen failure. Depending on the load to grain angle θ, the fracture, which occurs along the grain, develops under various combinations of shear and normal stresses. As an intermediate step, it is convenient to use Eq. (5.1) and Eq. (5.2) and express the failure condition Eq. (3.1) and Eq. (3.2) as an uniaxial failure function defining the relation between the axial stress at failure σ^F and the off-axis angle θ in terms of the strength parameters including f_{xy}:

$$\sigma^F = \pm \frac{f_{xy} f_x f_y}{\sqrt{c^4 f_{xy}^2 f_y^2 - c^2 s^2 f_{xy}^2 f_y^2 + c^2 s^2 f_x^2 f_y^2 + s^4 f_{xy}^2 f_x^2}} \tag{5.19}$$

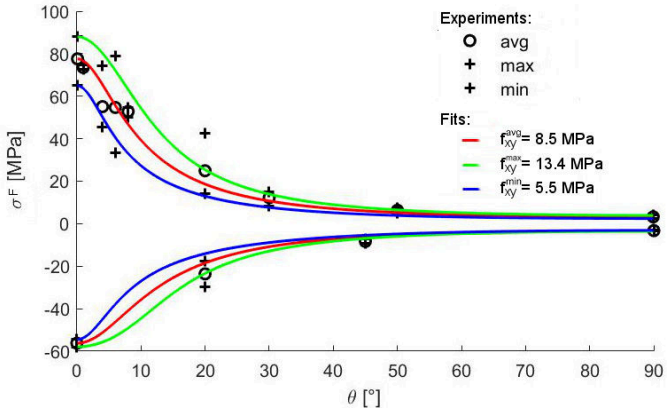

Figure 5.3: Calibration of the Tsai-Hill criterion parameter f_{xy} in terms of $\sigma^F(\theta)$ using the average, minimum or maximum values of the off-axis tension and compression test results f_x, f_{cx}, f_y, and f_{cy}.

Then, the optimal value of f_{xy} can be obtained by least-square fitting the uniaxial failure function to the experimental data of axial stress at failure vs. off-axis angle θ. In this procedure, the values of the remaining strength parameters f_x, f_{cx}, f_y, f_{cy} are kept constant and set to the averages, minima or maxima obtained in Section 5.2.1. As shown in Fig. 5.3, we fitted either the average, minimum or maximum experimental data, which allowed us to obtain three corresponding values of f_{xy}^{avg}, f_{xy}^{min} and f_{xy}^{max}, respectively. The values and corresponding residuals are listed in Table 5.1.

It is worth noting that even f_{xy}^{min} is greater than f_{xy}^{ASTM}, which supports our previous argument regarding the interpretation of the ASTM test.

5.3 Crack-type criterion

The parameter θ_c was introduced in the model to distinguish the cases when fracture occurs across or along the grain. In the present off-axis tension tests we found that only some of the specimens belonging to the OT-0° and OT-1° batches, that is with actual θ in the range between 0° and 2°, exhibited rupture perpendicular to the grain, while all specimens of the other groups, that is with actual $\theta > 2°$, ruptured along the grain. Therefore, even though the exact value of θ_c could not be identified, it is in the range between $\theta = 0°$ and $\theta = 2°$. For illustration, the surface defined by the crack-type condition $F_{CT} = 0$ is displayed in 2D stress space in Fig. 3.1 for critical load-grain angle $\theta_c = 2°$.

5.4 Cohesive (traction-separation) law

As we have discussed in Chapter 3, the cohesive law characterizes the cohesive behavior of a crack once it forms and it is defined as the relationship between the cohesive traction and the relative displacement of the crack surfaces (crack opening or sliding displacement). It could be directly identified from the uniaxial tension test if the entire load-displacement curve including the post-peak branch up to complete separation of the specimen fragments was recorded. Unfortunately, as it is obvious from Fig. 4.3, in spite of controlling the tension tests by displacement, we were able to capture only the ascending part of the response curves. On the other hand, Fig. 4.15a shows that the softening behavior was recorded in the compact tension tests, at least for the case when the load was applied orthogonally to the grain and the crack propagated in mode-I along the grain (CT-90° group). This enabled us to identify the parameters of the $t_n(\delta_n, 0)$ function (Eq. (3.8)) for a crack parallel to the grain: t_n^{ci}, $\delta_{n,crit}$, c_1, c_2 by one of the following procedures: (1) trial-and-error variation of the cohesive law parameters in the inverse numerical simulation of the CT test described in Section 5.4.1 or (2) least-square fitting the cohesive law function $t_n(\delta_n, 0)$ (Eq. (3.8)) to the piece-wise linear representation of the traction-separation relation retrieved by numerical inverse analysis of the CT test [83], see Section 5.4.2. The first simpler approach is considered less precise compared to the other one, that is more robust. Nevertheless, the cohesive law parameters were used within validation of the material model while the parameters from the latter one were applied for predictive numerical simulations.

5.4.1 Trial and error approach

To obtain the parameters of the cohesive law (Eq. (3.8)), inverse numerical analysis of the compact tension tests was used. In these calculations, values of the elastic moduli and tensile strengths were set equal to the average values listed in Table 5.1 and the shear strength was set to the value f_{xy}^{avg} identified in Section 3.1. The cohesive law parameters $\delta_{n,crit}$, c_1, and c_2 were varied by the trial-and-error so as the lower, median, and upper response range of the CT experiment was reproduced. The overview of the identified parameters is given in Table 5.2. The experimental responses are given in Fig. 5.4 together with the numerical results from the FE inverse analysis.

As no suitable test data was available to determine the fracture properties of timber in the crack-tangent direction, the value of the critical tangent crack

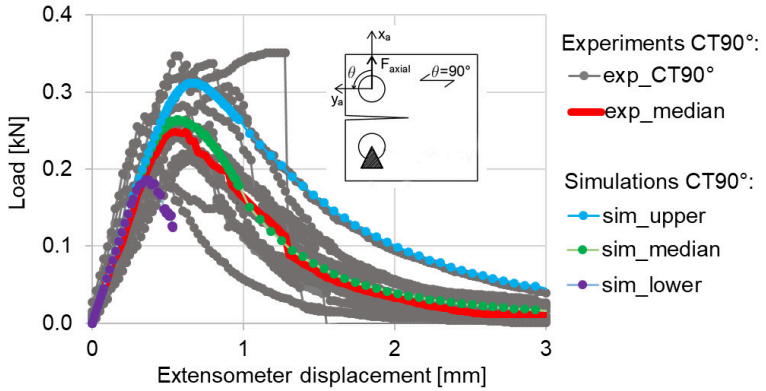

Figure 5.4: Calibration of the cohesive law parameters by trial-and-error variation: load vs. extensometer displacement for CT test with 90° load-grain angle for the curves from experiments (with their median curve) and numerical simulations.

CT test simulation	Failure surface	Cohesive law		
Fit range	f_{xy} [MPa]	$\delta_{n,crit}$ [mm]	c_1 [−]	c_2 [−]
lower		0.10		
median	8.5	0.42	3.00	6.50
upper		0.60		

Table 5.2: Calibration of the cohesive law parameters by trial-and-error variation: the inverse numerical analysis of the CT test.

displacement $\delta_{m,crit}$ and the material parameter p were set to $\delta_{m,crit} = 0.6$ mm and $p = 2$.

5.4.2 Systematic approach based on numerical inverse analysis

The inverse analysis of traction-separation (TS) relationship based on sequentially linear approach proposed by Vorel and Kabele [83] uses loading curve from a fracture test, e.g. prescribed force load vs. measured CMOD, as an input. Matching these variables to the experimental data during the finite element analysis, in which potential crack paths are modeled by interface elements, the corresponding TS relation for these elements is calculated. The agreement between the experimental data and the numerical analysis can be improved by the use of the multi-pass approach that captures the potential variability of cohesive fracture properties along the crack path.

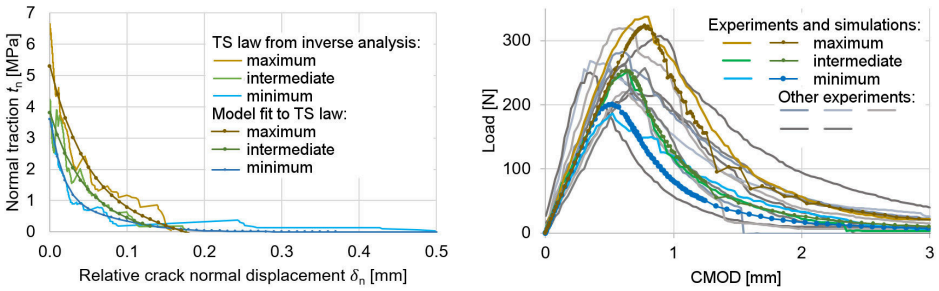

(a) (b)

Figure 5.5: Calibration of the traction-separation relation (Eq. (3.8)) using the results of CT-90° tests: (a) relation $t_n(\delta_n, 0)$ obtained by inverse analysis (no marker) and its fit by Eq. (3.8) (dot marker) and (b) load vs. CMOD relations from CT tests and their simulations. The color lines without marker indicate the experimental data representing the lower bound, intermediate range, and upper bound of the measured responses. The color lines with dot marker indicate results of the tests' numerical reproduction (validation).

It is to say, that the obtained TS relation has the form of a saw-tooth curve. For the purpose of the calibration of the proposed constitutive model, the TS relation needs to be further approximated by the Hordijk function [84] using the least-square method to become a suitable TS law input.

Firstly, we performed numerical inverse analysis of the CT test [83] to retrieve a piece-wise linear representation of the traction-separation relation (saw-toothed lines in Fig. 5.5a). To this end, a finite element model of the CT test with elastic parameters (E_x, E_y, G_{xy}) and Poisson's ratio (ν_{xy}) set equal to the average values listed in Table 5.1 was used. Secondly, the sought parameters t_n^{ci}, $\delta_{n,crit}$, c_1, c_2 were obtained by least-square fitting the $t_n(\delta_n, 0)$ function (Eq. (3.8)) to the raw traction-separation data. Once the $t_n(\delta_n, 0)$ relation was identified, we used Eq. (3.10) to evaluate the fracture energy G_f. The procedure was carried out for three measured load-CMOD curves representing the lower bound, intermediate range, and the upper bound of the bundle shown in Fig. 5.5b (colored lines). The corresponding curves and values are denoted as "minimum", "intermediate", "maximum" in Fig. 5.5 and Table 5.3. To validate the results, we performed a forward finite element simulation of the CT test using the $t_n(\delta_n, 0)$ model with the identified values of the parameters (Table 5.3). As seen in Fig. 5.5b, the calculated load-CMOD curves approximate well the experimental data proving validity and accuracy of the applied method. From the definition of the cohesive law (Eq. (3.8)) it is obvious, that for a pure mode-I cracking parallel to the grain, the stress at crack initiation t_n^{ci} should correspond with the uniaxial tension strength f_{ty}. By comparing the respective values in Table 5.1 and Table 5.3, we can see that $t_n^{ci} = 3.6$ MPa obtained for the lower bound fit to the CT data is close to the average value of $f_{ty} = 3.2$ MPa from the OT-90° tests. This observation can be explained by considering that the strength in the uniaxial tension test

CT test	Cohesive law				Fracture energy	Goodness of fit
Fit response	t_n^{ci} $[MPa]$	$\delta_{n,crit}$ [mm]	c_1 [–]	c_2 [–]	G_f [N/m]	R^2 [–]
Minimum	3.6	0.52	8.8	21.5	124.1	0.91
Intermediate	3.8	0.18	1	3.7	170.9	0.94
Maximum	5.3	0.20	1.0	3.7	246.8	0.92

Table 5.3: Values of the cohesive law parameters calibrated to the minimum, intermediate, and maximum response of the CT-90° test results.

is determined by the weakest cross-section in the dog bone specimen, while in the CT test the fracture path, which is predetermined by the notch, may not "hit" the weakest link in the sample. Therefore, we recommend to use the cohesive-law parameters corresponding to the lower bound of the CT data for calculations with the model outlined in Chapter 3. We should remark that in spite of experimenting with various test configurations (Chapter 4), we were unable to retrieve reliable data for the post-cracking softening behavior, which would allow us to identify, either directly or through inverse analysis, the parameters of the cohesive law for the shear traction component $t_m(0, \delta_m)$ and for cracking perpendicular to the grain.

5.5 Partial summary

While calibration of some parameters, such as elastic moduli, was straightforward, identification of other model components required more involved procedures:

- For the Tsai-Hill failure surface, defining the stress state for crack initiation, we used the least square method to fit the off-axis test results.
- For the crack-type criterion, which determines whether the crack occurs across or along the fibers, we estimated the critical load-grain angle by the visual inspection of the failed off-axis tensile test. However, this approach provided only bounds for the parameter values. Thus, this value has to be further refined to alleviate divergence problems of the finite element non-linear solution.
- For the cohesive law, defining the softening response of a crack, we applied (1) the trial and error approach to inverse numerical analysis and (2) the systematic approach based on numerical inverse analysis to the compact tension test results for the crack-normal direction.

Chapter 6

Validation of the model

6.1 Introduction

This chapter, adapted from [36], describes the numerical analysis of the three-point bending test of glued laminated timber arches with the fibers aligned with the longitudinal direction depicted in Section 4.8. The prime objective of the simulations discussed hereafter was to validate the constitutive model (overviewed in Chapters 3 and 5), and to demonstrate its capacity to predict the fracture phenomena that occur in timber under complex and non-proportionally evolving stress states. To this end, we used the model with parameters identified from material tests (summarized in Section 5.4.1, Table 5.1 and Table 5.2) to run finite element simulations of the tests on notched beams (described in Section 4.8). A nearly uniform mesh consisting of four-node quadrilateral plane-stress elements was used to discretize the timber arches (Fig. 6.1). The vertical notch was represented by a column of missing elements. As the material was orthotropic, the material axes were assigned to each element so as the grain direction was parallel to the arch longitudinal direction. Steel platens at the loading point and supports were modeled by elastic elements with high stiffness, perfectly bonded to the timber elements. The loading was applied as the prescribed vertical displacement with the magnitude of 25 mm. The loading point was placed at a small offset from the symmetry axis (2 % of the span) to incite the non-symmetric failure, which was observed in all the experiments due to a natural inhomogeneity of the material and inevitable imperfections of the setup. The material-non-linear calculations were performed incrementally using the Newton-Raphson method. To this end, the unit load magnitude

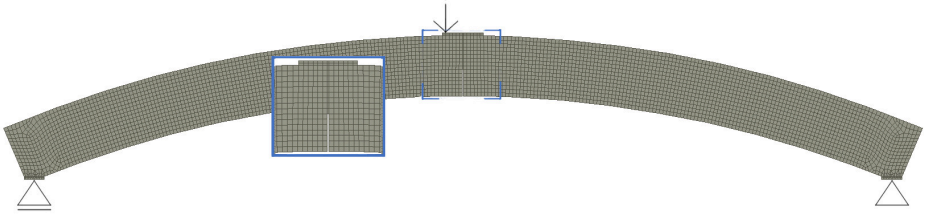

Figure 6.1: 2D FE mesh composed of approx. 7.5 mm by 7.5 mm quadrilaterals aligned with the arch longitudinal direction and lamina.

was scaled by a suitable loading factor.

6.2 Numerical solution aspects

To determine the appropriate element and loading increment sizes we used the model of the arch with the $0.5h$ notch. First, two models with meshes with typical element size of 3.7 mm and 7.5 mm were analyzed. The displacement-controlled loading was applied by equal increments with the loading factor of 0.15 (i.e., the actual load increment was 3.75 mm). Fig. 6.2 shows that both models yielded similar load-deflection curves up to the deflection of 30 mm, beyond which the calculation with the finer mesh was terminated due to its high computational demand. The inset in Fig. 6.2 also indicates that similar fracture patterns were obtained: the primary crack propagated along the grain from the notch tip followed by a secondary parallel crack developing above it. Therefore, it was concluded that the mesh with the element size of 7.5 mm provided a converged solution (with respect to the discretization) and that it would be used for all the subsequent analyses.

Secondly, the results of calculations with the incremental loading factor of 0.15 and 0.35 were compared. A good consistency of the load-displacement relations is obvious from Fig. 6.2. The final crack patterns are also similar, although with the larger step, the propagation of the secondary crack is less extensive. We attribute this to the fact that the secondary crack significantly extended during the final, softening, step of the calculation. As the equilibrium path exhibits bifurcations in the softening regime, the larger increment might have "overshot" some of the equilibrium states with more elements cracked. Throughout the calculations, we observed that after multiple elements cracked, the convergence of the non-linear solution was slow, typically requiring about 70 iterations. We also found that with the initially estimated value of the threshold angle, which determines whether a crack forms along or across the grain, $\theta_c = 1°$, the calculation often diverged due to some isolated elements

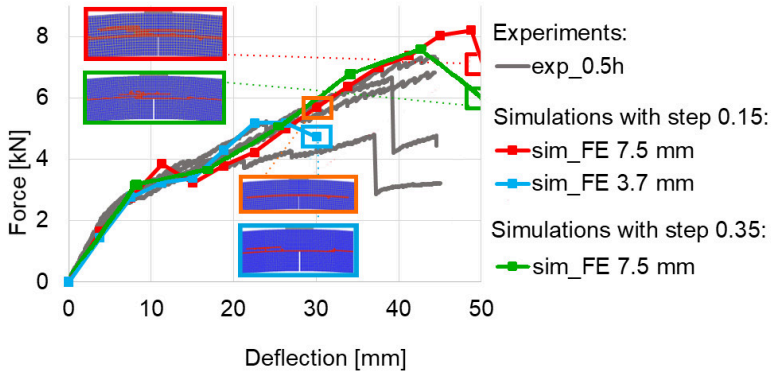

Figure 6.2: Experimentally and numerically obtained load-deflection curves for the arches with the vertical notch of $0.5h$.

oscillating between the two states. This problem was alleviated by setting $\theta_c = 0.001°$. As the value of this parameter was experimentally identified only as $\leq 1°$, this modification was accepted.

6.3 Comparison against experiments

Let us pay attention again to Fig. 6.2, which also allows us to compare the calculated results with the experimental ones. We can see two distinct trends among the experimental curves. Two curves show a monotonous hardening up to the deflection of 45 mm, when the experiment was terminated. The initial change of slope was associated with the formation and growth of the primary crack extending from the notch tip (Fig. 4.22a). No other major crack developed in this case. The other two curves show pronounced drops at the deflection between 35 and 40 mm. These drops occurred due to branching of the primary crack and formation of the secondary parallel cracks seen open in Fig. 4.22b.

The simulation result, calculated with the coarser mesh and the loading factor of 0.35, follows the monotonic experimental curves, but it exhibits a softening drop at the deflection of $43 - 50$ mm. As discussed earlier this drop was connected with the extension of the secondary crack.

Thus, we can state that the simulation well reproduced the experiments in terms of the load-deflection curves and the occurrence of the primary crack. It also captured the structural failure due to formation of the secondary cracks, as well as these cracks' location.

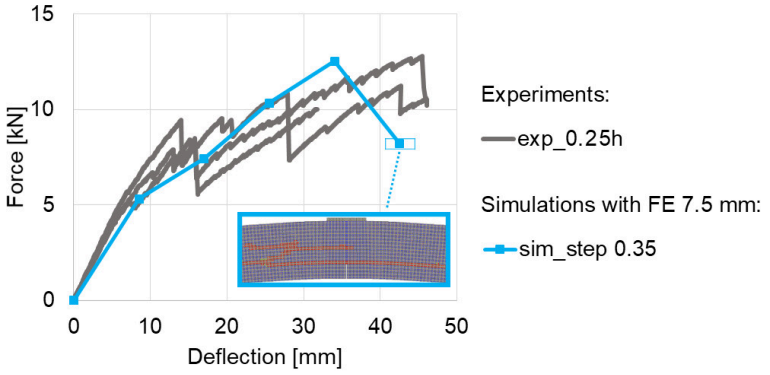

Figure 6.3: Experimentally and numerically obtained load-deflection curves for the arches with the vertical notch of $0.25h$.

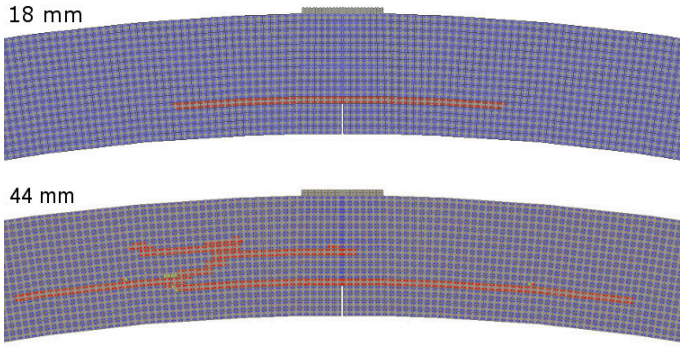

Figure 6.4: Crack patterns calculated for the arch with $0.25h$ notch: at the deflection of 18 mm (upper) and 44 mm (lower).

We ran the simulation of the arches with $0.25h$ notch with the element size of 7.5 mm and the loading increment of 0.35, as discussed in Section 6.2. The resulting load-displacement curve is presented in Fig. 6.3 together with the experimental results. The latter curves show a monotonous hardening, associated with the initiation and the growth of the primary crack extending from the notch tip, up to the deflection of $14 - 28$ mm. In this deflection range, the drops occur due to branching of the primary crack and formation of the secondary parallel crack presented in Fig. 4.24. The experimental responses proceed with the final slope related to the secondary crack growth.

The simulation result follows the monotonic experimental curves. The softening drop occurs at the deflection of $34 - 43$ mm with the extension of the secondary crack. The crack pattern obtained by the calculation is shown in Fig. 6.4. We can see, that at the deflection of 18 mm, the primary crack initiated at the notch tip grows parallel to the grain up to the deflection of 44 mm where a secondary crack propagates above.

Similarly to the numerical results of the arches with $0.5h$ notch, we can see, that the simulation of the arches with $0.25h$ notch well reproduced the experiments. The load-deflection curves and the occurrence of the primary and the secondary cracks were adequately reproduced. The calculations also well captured the crack pattern observed in the experiments. To conclude, the numerical simulations of the arches with both $0.5h$ and $0.25h$ notch validated the model proposed by the author [15].

6.4 Partial summary

Using simulation of loading tests on notched GLT arches as an example allowed us to validate the proposed constitutive model.

An attention must have been paid to appropriate discretization of the problem into finite elements, especially when smeared approach is used to model cracks. However, as the crack cohesive law of underlying constitutive model is defined in terms of tractions and relative crack displacements (as opposed to strain) and the implementation properly accounts for element size [15], mesh objectivity was ensured, as shown in Section 6.2.

When material softening occurs, the problem of cracking/deformation localization and equilibrium path bifurcation arises. The results presented in this paper show that the model, in general, was able to predict localization of fracture to narrow bands of elements. However, as mentioned in Section 6.2, the localization patterns may be affected by the chosen load increment size. Even though only results with two increment sizes were presented, our experience was that excessively reducing the increment size may be counterproductive, as it often led to non-localized solutions and divergence. On the other hand, too large increments may miss some of the localized solutions. The present study validated the model [15] since:

- The simulations' results fit well the load vs. deflection curves of arch experiments with both notch lengths, when the average values of input parameters obtained from independent material tests were used.
- For the arches with the short and long single edge notch the simulations reproduced well the cracking process observed in experiments: (1) The primary crack that initiated at the notch tip and propagated along the grain. (2) The secondary crack consequently initiated above the primary

one in the middle fiber layer in the area above notch and grew also in the direction parallel to the grain.

Finally, it should be remarked that inherent inhomogeneities of natural materials like timber lead to significant variation in material characteristics. To obtain statistically significant material parameters of timber, numerous experiments must be conducted. In the present study, adequate results were obtained even though timber was idealized as perfectly homogeneous material and imperfection was introduced by slightly perturbing symmetry of the loading. However, the author is aware that a more systematic approach might, for example, consist in representing the statistical variation of material properties in the finite element model using random fields [85, 86].

Chapter 7

Predictive numerical analyses

In this chapter, extracted from [17], the results of the predictive numerical analyses of the ASTM shear and pre-stressed CT experiments, reported in Sections 4.5 and 4.6, are presented. The aim of this numerical study is to demonstrate further capabilities of the model and to shed light on the fracturing processes in different test configurations.

7.1 Numerical simulations of shear test

7.1.1 Introduction

The aim of the ASTM shear test simulations was to demonstrate the capability of the constitutive model outlined in Chapter 3 to reproduce the behavior of timber dominated by shear crack parallel to the grain. As the critical crack-sliding displacement $\delta_{m,crit}$ for the crack parallel to the grain is not known from the model calibration reviewed in Chapter 5, numerical simulations were run with different values from an estimated range. The mesh used for discretization of the timber shear blocks (Fig. 7.1) was regular consisting of four-node quadrilateral plane-stress elements with the size of approx. 2.5 mm by 2.5 mm. Only the elements along the shearing line had the width of 2.0 mm, which was used as the characteristic length parameter l_{ch} for the crack parallel to the grain. As the material was orthotropic, the material axes were assigned to each element so as the grain direction was parallel

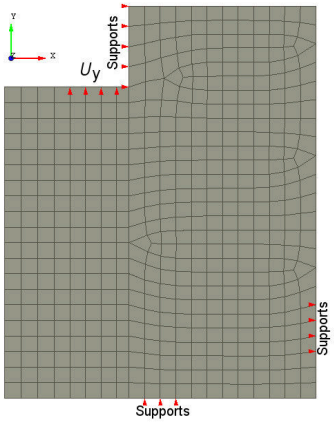

Figure 7.1: 2D FE mesh composed of approx. 2.5 mm by 2.5 mm quadrilaterals aligned with the specimen longitudinal direction and lamina.

to the specimen longitudinal direction. The vertical displacement U_y with the unit magnitude of $U_y^0 = 0.1$ mm was prescribed in half of the nodes along the horizontal notch edge, except for the inner corner node enabling shearing of the column of elements. This unit load magnitude was scaled by an appropriate incremental loading factor, see Section 7.1.2. The vertical load plate that prevents the specimen from rotation was modelled as prescribed supports $U_x = 0$ mm along the vertical notch edge. Similarly, the base plate and the crossbar were considered as the supports $U_y = 0$ mm and $U_x = 0$ mm, respectively. The zero vertical displacement was prescribed only in the nodes placed further from the base plate - crossbar corner to minimize the effect of friction. The material-non-linear calculations were performed using the Newton-Raphson method.

7.1.2 Numerical solution aspects

The element size and loading increment magnitude were determined by the numerical analyses of two models with meshes with typical element size of 2.5 mm and 1.0 mm. The mesh with 2.5 mm element size was used to compare the incremental loading factor of 0.15 and 0.30, that is the actual load increment of 0.015 mm and 0.030 mm, respectively. The results in Fig. 7.2 show that the load-relative displacement curves are similar for both models up to the relative displacement of $\Delta_{x,DIC} = 0.175$ mm, where the finer mesh calculation was ended due to exceeded convergence criteria. The obtained fracture patterns were also similar: the crack parallel to the grain spread from the notch edge downwards along the shearing line towards the compression-shear zone with non-linear deformation around the edge of the bottom support. A partial conclusion was drawn to be used for all the

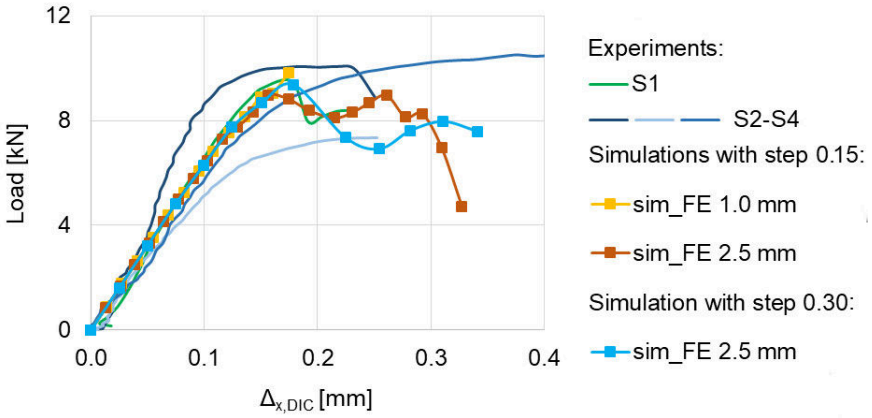

Figure 7.2: The effect of element size and load step size on calculated response in the shear test simulation.

subsequent analyses, that the mesh with the 2.5 mm element size provided a converged solution. Comparing the calculation results with the incremental loading factor of 0.15 and 0.30, we can see a good agreement in responses and crack patterns.

7.1.3 Results

First, in Fig. 7.3, we compare the experimental results with the numerical responses obtained with the intermediate parameters in Table 5.3 for different values of critical crack-sliding displacement $\delta_{m,crit} = \{0.03, 0.055, 0.100, 0.600\}$ mm. We can see, that the model reproduces well the initial slope, the post-peak branch, and the lowest, intermediate, and the highest level of the load capacity observed in tests. We can notice, that the results with $\delta_{m,crit} = \{0.100, 0.600\}$ mm yield almost the same response and the parameter $\delta_{m,crit} \geq 0.100$ mm does not influence the responses.

Second, in Fig. 7.4, we compare the experimental results with the numerical responses obtained with $\delta_{m,crit} = 0.055$ mm and the minimum, intermediate, and maximum parameters from Table 5.3. The calculations with the minimum and the intermediate parameters reproduce well the S1 experiment, as for the peak value followed by a decrease, hardening and a final drop. They differ only in the final drops that occur beyond $\Delta_{x,DIC} = 0.2$ mm and $\Delta_{x,DIC} = 0.26$ mm, respectively. Compared to it, the calculation with the maximum parameters reproduce well the S2 and S4 experiment exhibiting the plateau followed by the final drop.

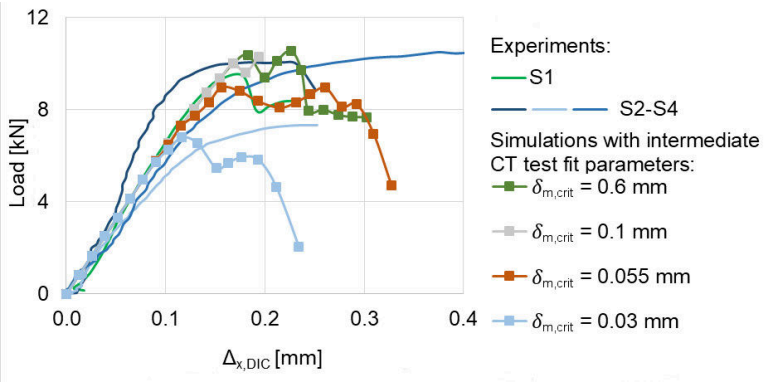

Figure 7.3: Load vs. DIC relative vertical displacement $\Delta_{x,DIC}$ for the results of ASTM shear test experiments and simulations calculated with the intermediate parameters from Table 5.3 and different values of $\delta_{m,crit}$.

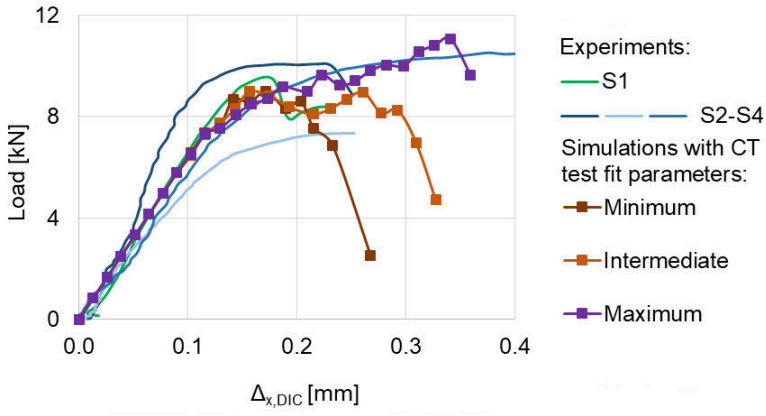

Figure 7.4: Load vs. DIC relative vertical displacement $\Delta_{x,DIC}$ for the results of ASTM shear test experiments and simulations calculated with the minimum, intermediate, and maximum parameters from Table 5.3 and $\delta_{m,crit} = 0.055$ mm.

As expected, a similar crack pattern occurred in the numerical simulations: the crack parallel to the grain initiated under tensile-shear stress states at the upper edge of the shearing area propagating downwards. A zone, in which the non-linear deformation was developing under compression and shear, spread upward from the lower support along the shear plane until it reached the downward-growing crack, see Fig. 7.5a. The final strain states ε_{xx} and γ_{xy} are shown in Fig. 7.5b and Fig. 7.5c, respectively. Comparing the strain states with the image of cracking at the maximum relative vertical displacement in Fig. 4.10, we can see, that the model captures the crack pattern adequately.

As overviewed in Section 4.5, the shear strength according to the ASTM standard f_{xy}^{ASTM} is calculated by dividing the maximum attained force F_{max} and the shearing area A. Therefore, it corresponds to the average shear stress

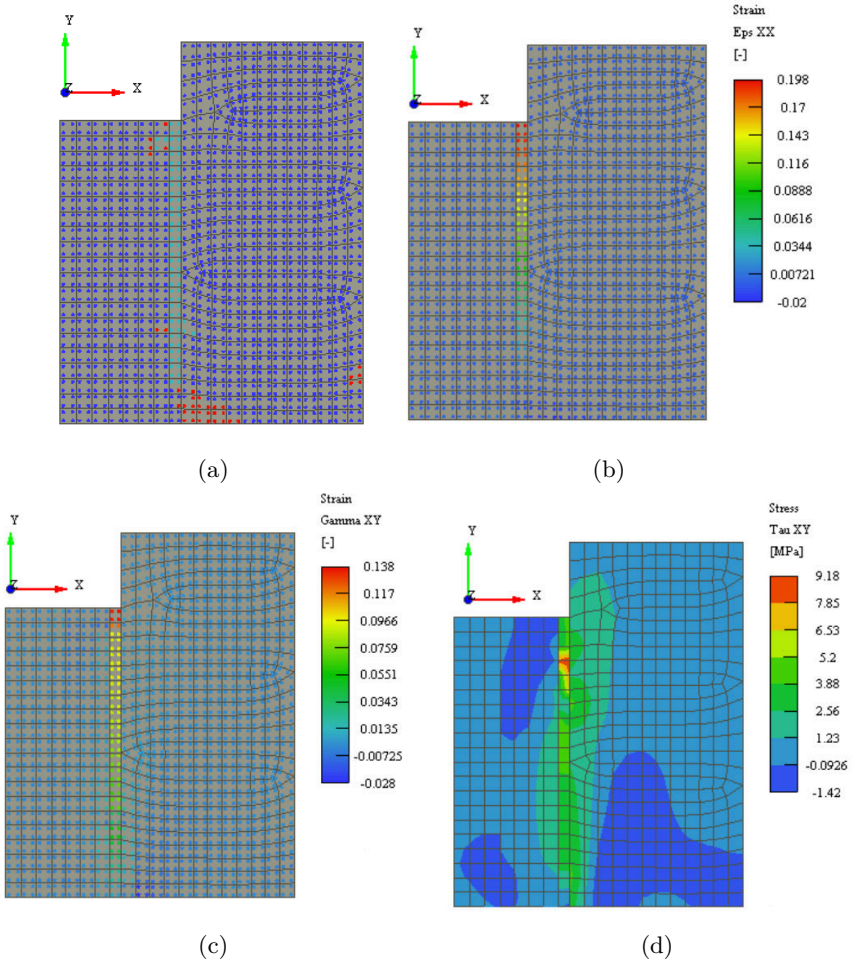

Figure 7.5: ASTM shear test simulation result at (a-c) $\Delta_{x,DIC} = 0.3$ mm and (d) $\Delta_{x,DIC} = 0.16$ mm for intermediate parameters from Table 5.3 and $\delta_{m,crit} = 0.055$ mm: (a) crack parallel to the grain (red) and non-linear deformation zone (green) developed under compression and shear stress states, (b) normal strain ε_{xx}, (c) shear strain γ_{xy}, and (d) shear stress τ_{xy}.

on the area at the specimen failure. The Fig. 7.5d shows the shear stress along the shearing area around the peak load at $\Delta_{x,DIC} = 0.16$ mm.

7.2 Numerical simulations of pre-stressed CT test

7.2.1 Introduction

The main objectives of the pre-stressed CT test simulations were to demonstrate the capability of the constitutive model outlined in Chapter 3 to reproduce the behavior of timber dominated by tensile crack parallel or perpendicular to the grain or combination of both, i.e., the failure modes F0-F2. Based on the results from Section 7.1.3, the parameter $\delta_{m,crit} = 0.055$ mm for the crack along the grain was used in pre-stressed CT test simulations. As the cohesive law parameters for the crack across the grain are not known from the model calibration reviewed in Chapter 5, numerical simulations were run with assumed values of critical crack-opening and sliding displacements $\delta_{n,crit}^{across} = 1.1$ mm and $\delta_{m,crit}^{across} = 1.1$ mm, and parameters $c_1^{across} = 3.0$ and $c_2^{across} = 6.7$.

The pre-stressed CT specimens were discretized with a regular mesh consisting of four-node quadrilateral plane-stress elements with the size of approx. 2.0 mm by 2.0 mm (to model the specimen and confinement plattens) and four external cable elements (to induce the confinement), see Fig. 7.6. The axes of the orthotropic timber material were assigned to each element so as the grain direction was perpendicular to the direction of the specimen's notch.

The loading was applied as the vertical displacement U_y with the unit magnitude of $U_y^0 = 0.01$ mm to the upper loading hub as shown in Fig. 7.6. This unit load magnitude was scaled by an incremental loading factor specified in Section 7.2.2. The loading point was placed at a small vertical offset of 4 mm from the loading hub's centroid to enhance the non-symmetric failure as observed in the experiments. The bottom hub was fixed at its center. The material-non-linear calculations were performed using the Newton-Raphson method.

7.2.2 Numerical solution aspects

Using two models with meshes with typical element size of 2.0 mm and 1.0 mm, the appropriate element size and loading increment magnitude were determined. The mesh with 2.0 mm elements was used to run calculations

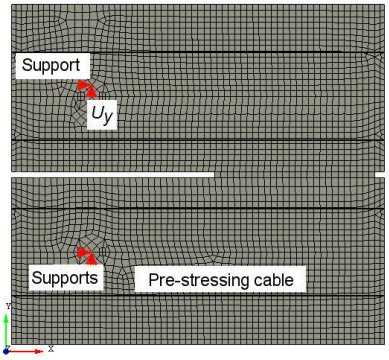

Figure 7.6: 2D FE mesh composed of approx. 2.0 mm by 2.0 mm quadrilaterals aligned with the specimen edges.

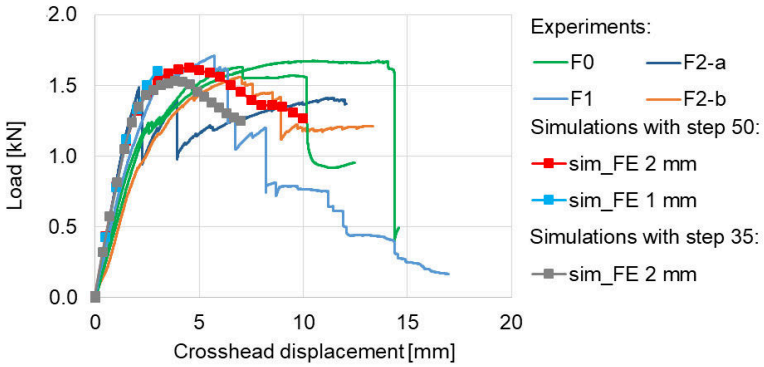

Figure 7.7: The effect of element size and load step size on calculated response in the CT test simulation with the pre-stress of 3.3 MPa, $\theta_c = 1.6°$, and failure type F1.

with the incremental loading factor of 50 and 35, that is the actual load increment of 0.50 mm and 0.35 mm, respectively. As seen in Fig. 7.7, the load-crosshead displacement curves were similar for both models up to the displacement of 3.0 mm, where the calculation with the finer mesh ended due to exceeded convergence criteria. The obtained fracture patterns were similar, both of the type F1 - fibers' rupture concentrated around or at the cross-section ahead of the notch. It was concluded that the mesh with 2.0 mm element size provided a converged solution and, thus, can be used for all subsequent calculations. Comparing the calculation results with the incremental loading factor of 50 and 35, we can see a good agreement in responses in Fig. 7.7 and the same can be said about the crack patterns. The slight difference in slope of the softening branches is attributed to the fact that the disintegration of the fibers' bundles, that accompanied fibers' rupture along the ligament within the failure type F1, occured at different locations and had a different extent in each calculation.

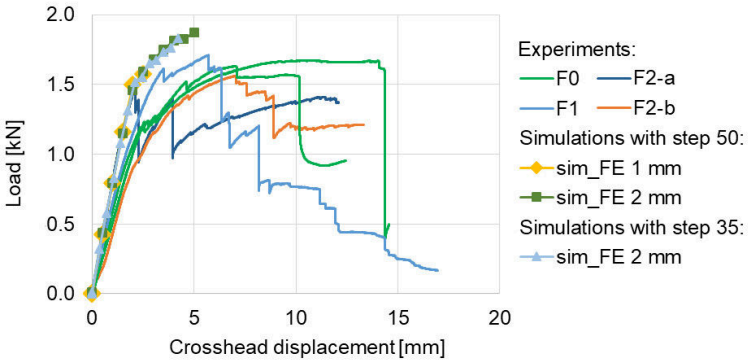

Figure 7.8: The effect of element size and load step size on calculated response in the CT test simulation with the pre-stress of 3.3 MPa, $\theta_c = 0.4°$, and failure type F0.

To confirm that the element size of 2.0 mm and the loading increment of 0.50 mm are also suitable for other failure types, numerical analysis similar to the previous one (Fig. 7.7) was conducted with the critical load-grain angle of $\theta_c = 0.4°$ which hindered propagation of the main crack across the grain in the notch direction and encouraged failure due to vertical cracking along the grain (type F0) - see also the discussion in Section 7.2.4. The results in Fig. 7.8 show that both models yielded similar response up to the displacement of 2.5 mm, where the finer mesh calculation ended due to exceeded convergence criteria. The obtained fracture patterns were very similar, both categorized as failure type F0. The comparison of the simulations with the incremental loading factor of 50 and 35 showed a very good agreement in responses and crack patterns.

7.2.3 Results

Results of the calculations with pre-stress levels of 3.3, 3.0, 2.7, and 2.1 or 1.0 MPa are summarized in Fig. 7.9 and Fig. 7.10. Fig. 7.10 displays the normal strains ε_{xx} and ε_{yy}. Concentrations of these strains occur due to opening of horizontal (ε_{yy}) or vertical (ε_{xx}) cracks; therefore their contour plots indicate the crack patterns, which can be compared with those observed in experiments and shown in Fig. 4.14 and Fig. 4.13.

In the simulation with pre-stress of 3.3 MPa we observed propagation of a major crack across fibers in the direction of the notch (Fig. 7.10a top) with multiple short branches along the grain (Fig. 7.10a bottom). This pattern corresponds well with the failure type F1 seen in Fig. 4.14a. The respective load-displacement curve (Fig. 7.9) exhibits the highest peak and post-peak

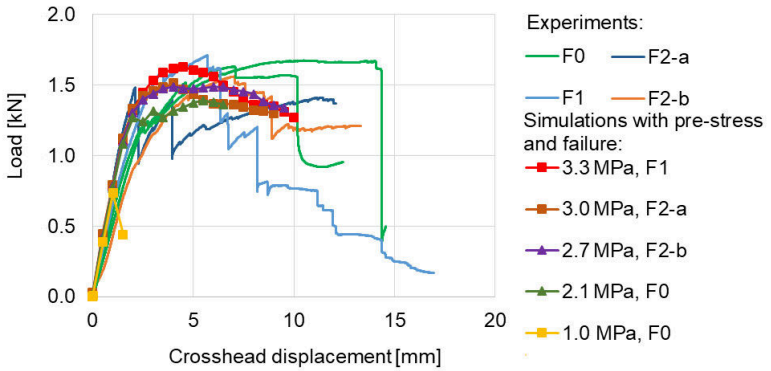

Figure 7.9: Load vs. crosshead displacement for the results of CT test experiments and simulations calculated with $\theta_c = 1.6°$ and different pre-stress levels.

softening. In the simulation with 3.0 MPa, crack across fibers propagated in the direction of the notch up to approx. one third of the ligament's length (Fig. 7.10b bottom) from where crack along the grain started to propagate (Fig. 7.10b top). Such a cracking corresponds to failure type F2-a shown in Fig. 4.14b. The calculated load-displacement response (Fig. 7.9) reaches the second highest peak, out of the curves for different pre-stress levels, followed by post-peak softening, hardening, and then a decrease at the end. In the simulation with 2.7 MPa, a major crack across fibers (Fig. 7.10c bottom), that propagated in the direction of the notch, was accompanied by the first branch along fibers (initiated at the notch tip) and followed by the second branch along fibers (initiated at approx. one half of the ligament's length), see Fig. 7.10c top. This cracking resembled failure type F2-b shown in Fig. 4.14c. The obtained load-displacement curve (Fig. 7.9) has the third highest peak followed by post-peak softening, hardening, and a decrease at the end. Crack along the grain initiated at or around the notch tip dominated in the calculations with 2.1 MPa and 1.0 MPa (Fig. 7.10d top). Nevertheless, it was accompanied by crack across the grain in a few finite elements at the ligament's beginning (Fig. 7.10d bottom) with crack-normal strain (i.e. ε_{yy}) much lower than that of crack along the grain (i.e. ε_{xx}). Such failure was considered comparable to failure type F0 presented in Fig. 4.13a. The obtained load-displacement curves are shown in Fig. 7.9 with the fourth and fifth highest calculated peak. For the calculation with 2.1 MPa, the peak is followed by post-peak hardening and a decrease at the end. For the simulation with 1.0 MPa, the post-peak branch is softening.

It is obvious that the numerical calculations were able to reproduce the different failure patterns (F0-F2) observed in the experiments. The models also captured well the initial slope, the peak, and the post-peak trends of the load-displacement records.

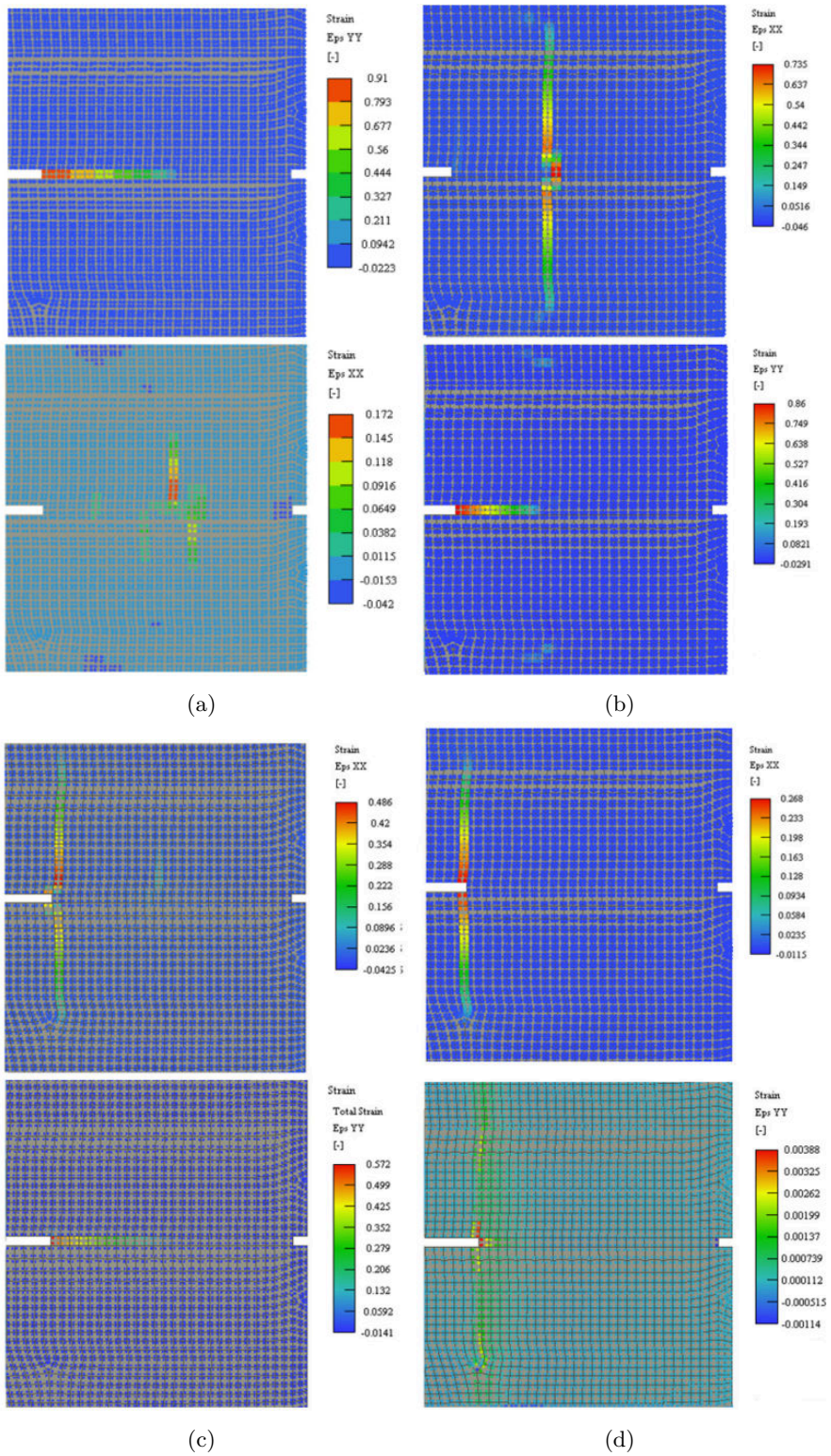

Figure 7.10: Distributions of normal strains ε_{xx} and ε_{yy} obtained from the CT test simulations with different pre-stress levels: (a) pre-stress 3.3 MPa (state at $U_y = 7.0$ mm), (b) pre-stress 3.0 MPa (state at $U_y = 9.0$ mm), (c) pre-stress 2.7 MPa (state at $U_y = 7.0$ mm), and (d) pre-stress 1.0 MPa (state at 1.5 mm).

7.2.4 Effect of threshold angle θ_c

The value of the threshold angle θ_c, which determines if a crack forms across the grain (splinter failure) or along grain, could not be exactly determined from uniaxial tension tests [35]. The tests only indicated that it falls within the range between 0° and 2°. Therefore, to investigate how sensitive is the model of the CT test to this parameter, two more sets of calculations were run with different values of $\theta_c = 0.4°$ and $\theta_c = 1.4°$. Results are summarized in Fig. 7.11 and Fig. 7.12.

In both sets of simulations with pre-stress of 1.0 MPa - 3.3 MPa, we observed a major crack along the grain initiated at or around the notch tip (Fig. 7.12 top), that was accompanied by a short branch, which propagated from the notch tip in the direction of the notch, either as crack along the grain for $\theta_c = 0.4°$ (Fig. 7.12a bottom) or crack across the grain for $\theta_c = 1.4°$ (Fig. 7.12b bottom). This crack pattern is considered to correspond well with the failure type F0 shown in Fig. 4.13a. All the load-displacement curves (Fig. 7.11) reach the peak with respect to the pre-stress level. The post-peak behavior exhibits hardening, except for the calculation with 1.0 MPa in which softening occurs.

To summarize the CT test simulations with regard to critical load-grain angle θ_c and pre-stress level, different failures were observed:

- type F0 occurred with $\theta_c = 1.6°$ and the pre-stress level of 1.0 MPa and 2.1 MPa or with $\theta_c = 0.4°$ and 1.4° and all the pre-stress levels of 1.0 MPa to 3.3 MPa,
- type F1 with $\theta_c = 1.6°$ and 3.3 MPa,
- type F2-a with $\theta_c = 1.6°$ and 3.0 MPa,
- type F2-b with $\theta_c = 1.6°$ and 2.7 MPa.

The simulations with the pre-stress level of 2.7 MPa to 3.3 MPa and $\theta_c = 1.6°$ reproduced well the peak load, post-peak behavior, and respective failure types F1 - F2 (Fig. 7.9), that were observed in three experimental results out of five. Compared to it, the simulations with the same pre-stress level range and $\theta_c = 0.4°$ or $\theta_c = 1.4°$ reproduced adequately the load capacity, post-peak hardening, and respective failure type F0 (Fig. 7.11), that were observed in two experiments out of five. Based on experimental and numerical results, the following recommendation was drawn up: to

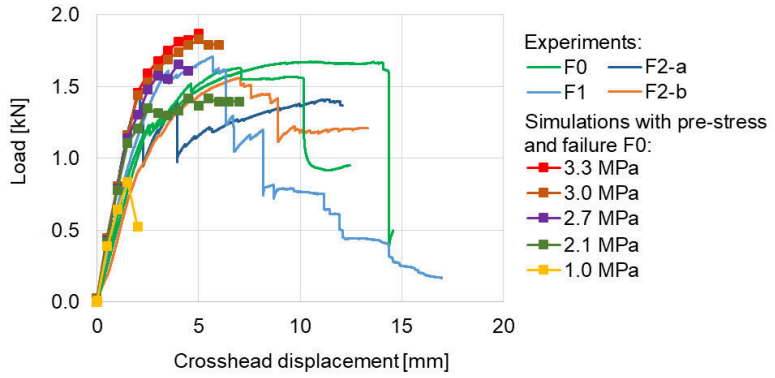

(a)

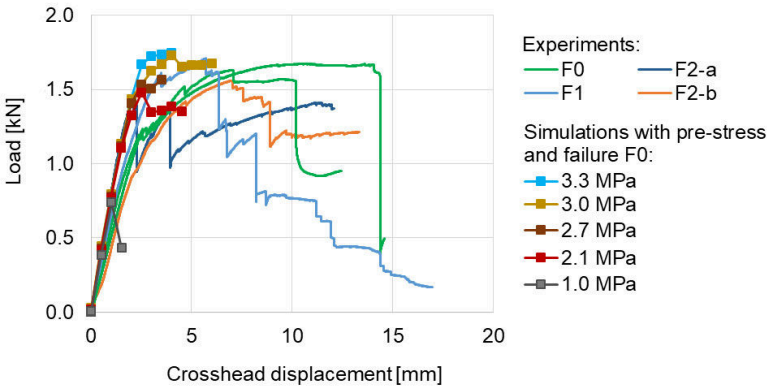

(b)

Figure 7.11: Load vs. crosshead displacement for the results of CT test experiments and simulations calculated for different pre-stress levels with (a) $\theta_c = 0.4°$ and (b) $\theta_c = 1.4°$ leading to failure type F0.

use $\theta_c = 1.6°$ and $\theta_c = 1.4°$ or less in 60% and 40% of pre-stressed CT test simulations, respectively, for a pre-stress level from the range between 2.7 MPa and 3.3 MPa.

Treshold angle θ_c, determined as the interval between 0° and 2° by visual assessment of off-axis tension specimens [35], may be regarded as one of timber material characteristics, which are typical for a significant variability. Thus, statistically significant results of not only off-axis tension tests but also CT experiments with regard to failure type are needed together with an appropriate statistical approach to numerical models.

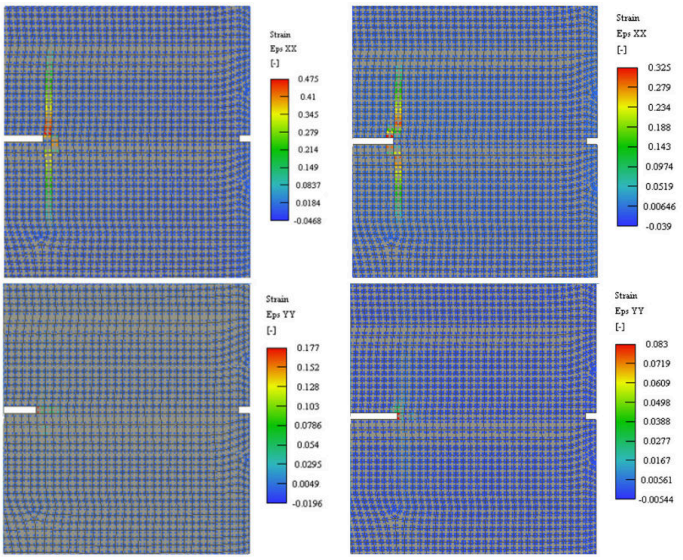

(a) (b)

Figure 7.12: CT test simulation result of normal strains ε_{xx} and ε_{yy} at crosshead displacement of (a) 4.0 mm and (b) 5.0 mm with the pre-stress level of 3.3 MPa and critical load-grain angle of (a) $\theta_c = 0.4°$ and (b) $\theta_c = 1.4°$.

7.3 Partial summary

The finite element method with an anisotropic constitutive model were used for numerical simulation of ASTM shear test and pre-stressed compact tension test. The numerical results reproduced adequately both the experimental responses and the crack patterns.

It was shown in shear test simulation that the value of the parameter f_{xy}^{ASTM}, obtained from $f_{xy}^{ASTM} = \frac{F_{max}}{A}$, represents the averaged stress at the failure plane, while the extreme stress locally experienced by the material is much higher. It is concluded that, if a finite element model of a structural member has a finer resolution of the stress field variation than is the size of the tested specimen, using the result of the ASTM shear test as the material strength may lead to underestimation of the member's load capacity.

The pre-stressed CT test simulation demonstrated the capability of the constitutive model to reproduce complex tensile-shear behavior of timber governed by tensile crack parallel or perpendicular to the grain or combination of both. The influence of the treshold principal load-grain angle θ_c to the results was analysed.

Chapter 8

Conclusion

Against the background of an overview provided on typical timber behavior, current timber models, and failure criteria suitable for timber, the two-dimensional homogeneous constitutive model for timber fracture under tensile and shear loads is depicted. The model has been enhanced, elaborated, and implemented in a finite element program by the author [15, 36]. In the model, three key rules are established for timber response:

- pre-cracking response is governed by elastic orthotropic behavior,
- crack initiation is governed by failure criterion accounting for orthotropy, which is accompanied by crack type criterion that distinguishes the formation of a crack parallel or perpendicular to the grain,
- post-cracking softening response is modeled by the fixed smeared crack approach [42] with regard to orthotropy. [15]

The model also captures unloading and reloading phenomena.

To acquire a consistent set of experimental data for calibration and validation of a material model capable of capturing complex timber behavior in both linear and non-linear range of the response under various stress combinations, an experimental campaign has been conducted. It was focused on the fracture behavior that initiated under tensile-shear stress states and the experiments included off-axis tension and compression tests, ASTM shear test, compact tension test with the load-grain angle of 0° and 90°, and three-point bending tests of single edge notched beams and arches.

The methodology of the model calibration using the obtained data is demonstrated:

- Moduli of elasticity in direction parallel and perpendicular to the grain (E_x, E_y), shear modulus (G_{xy}), Poisson's ratios (ν_{xy}, ν_{yx}), and tensile and compressive strengths in direction parallel and perpendicular to the grain (f_{tx}, f_{ty}, f_{cx}, f_{cy}) were evaluated using off-axis tension and compression tests results.
- The shear strength parameter (f_{xy}) was estimated in the scope of failure surface calibration, in which off-axis tension and compression tests results were applied.
- The range of treshold principal load-grain angle θ_c was retrieved from the calibration of crack-type criterion. To this end, the failure types of off-axis tension specimens were visually assessed.
- Traction-separation law parameters in crack-normal direction for the crack parallel to the grain, such as critical crack opening displacement ($\delta_{n,crit}$) and parameters of the Reinhardt-Hordijk function (c_1, c_2), were evaluated by trial and error approach or systematic approach based on numerical inverse analysis. For both of them, the results of compact tension test with the load-grain angle of 90° were used. [15]

The model has been successfully validated against experimental data from the three-point bending test of single edge notched arch [36]. The model reproduced well the load vs. deflection curves of arch experiments with the notch length of 0.25 and 0.5 times the cross-section height. Furthermore, the numerical simulation captured both (1) the primary crack that initiated at the notch tip and propagated along the grain and (2) the potential secondary crack initiated above the primary one in a fiber layer above the notch that grew also in the direction parallel to the grain.

To demonstrate capacity of the model to predict the fracture behavior of timber under complex loading states, predictive numerical simulations of ASTM shear test and pre-stressed compact tension test with the load-grain angle of 0° were conducted [17]. Within these simulations, the parameter of critical crack sliding displacement ($\delta_{m,crit}$) for the crack parallel to the grain and the traction-separation law parameters for the crack perpendicular to the grain were estimated. Also, the parameter of treshold principal load-grain angle θ_c was specified. The numerical results reproduced adequately both the experimental responses and the crack patterns.

The shear test simulations captured well the crack parallel to the grain that propagated along the expected shearing area. It was shown, that the

value of the shear strength parameter, obtained from ASTM shear test as the maximum attained force divided by the shearing area, represents the averaged stress at the failure plane, while the extreme stress locally experienced by the material is much higher. Therefore, the use of the ASTM shear test results as the material strength may lead to underestimation of the member's load capacity. [17]

The pre-stressed compact tension test simulation has shown that the constitutive model was able to reproduce complex tensile-shear behavior of timber where one or both of the crack types, i.e. tensile crack parallel and perpendicular to the grain, were involved. The influence of the treshold principal load-grain angle θ_c to the results was analysed. [17]

Appendix A

Bibliography

[1] A. Buchanan, *Structural Design for Fire Safety*. Hoboken, United States: John Wiley and Sons Ltd, 2001.

[2] J. Bodig and B. Jayne, *Mechanics of wood and wood composites*. Krieger Publishing Company, 1993.

[3] A. International, *ASTM D143-94 Standard Test Methods for small clear specimens of timber*. West Conshohocken: ASTM international, 2000.

[4] S. Holmberg, K. Persson, and H. Petersson, "Nonlinear mechanical behaviour and analysis of wood and fibre materials," *Computers & structures*, vol. 72, no. 4, pp. 459–480, 1999.

[5] P. Mackenzie-Helnwein, J. Eberhardsteiner, and H. A. Mang, "A multi-surface plasticity model for clear wood and its application to the finite element analysis of structural details," *Computational Mechanics*, vol. 31, pp. 204–218, May 2003.

[6] E. Serrano, *Adhesive joints in timber: modelling and testing of fracture properties*. PhD thesis, Lund University, Lund, Sweden, 2000. OCLC: 46387186.

[7] E. Serrano and P. J. Gustafsson, "Fracture mechanics in timber engineering – Strength analyses of components and joints," *Materials and Structures*, vol. 40, no. 1, pp. 87–96, 2006.

[8] H. R. Valipour and K. Crews, "Efficient finite element modelling of timber beams strengthened with bonded fibre reinforced polymers," *Construction and Building Materials*, vol. 25, pp. 3291–3300, Aug. 2011.

[9] J. Eberhardsteiner, M. Gingerl, L. Ondris, and R. Beer, "Experimental investigation of the strength of anisotropic solids under biaxial loading oblique to the principal material directions," *Communications - Scientific letters of the University of Zilina*, vol. 2, pp. 4–7, Sept. 2000. Number: 3.

[10] N. Khorsandnia, H. R. Valipour, and K. Crews, "Nonlinear finite element analysis of timber beams and joints using the layered approach and hypoelastic constitutive law," *Engineering Structures*, vol. 46, pp. 606–614, Jan. 2013.

[11] H. Yoshihara and M. Ohta, "Estimation of the shear strength of wood by uniaxial-tension tests of off-axis specimens," *Journal of Wood Science*, vol. 46, no. 2, pp. 159–163, 2000.

[12] C. Woodward and J. Minor, "Failure theories for Douglas-fir in tension," *Journal of Structural Engineering*, vol. 114, no. 12, pp. 2808–2813, 1988.

[13] B. P. Clouston, F. Lam, and J. D. Barrett, "Interaction term of Tsai-Wu theory for laminated veneer," *Journal of Materials in Civil Engineering*, pp. 112–116, 1998.

[14] R. Todeschini, *Uniaxial and biaxial tests for avaliation of failure criterion of anisotropic material applied to wood*. PhD thesis, Faculdade de Engenharia Civil, Arquitetura e Urbanismo, Campino, Brasil, 2009.

[15] E. Šmídová and P. Kabele, "Constitutive Model for Timber Fracture under Tensile and Shear Loads," *Applied Mechanics and Materials*, vol. 784, pp. 137–144, Aug. 2015.

[16] J. Červenka, L. Jendele, and V. Červenka, "ATENA Program Documentation, part 1, Theory," 2008.

[17] E. Šmídová and P. Kabele, "Finite element simulation of shear and compact tension tests on timber," *Acta Polytechnica CTU Proceedings*, vol. [In preparation], 2021.

[18] E. Šmídová, P. Kabele, and M. Šejnoha, "Response and damage evolution of single edge notched timber beams under three-point bending," *Acta Polytechnica CTU Proceedings*, vol. 26, pp. 94–99, 2019.

[19] CEN, *EN 408:1995 - Timber structures – Structural timber and glued laminated timber – Determination of some physical and mechanical properties*. Brussels: CEN, 1995.

[20] CEN, *EN 1995-1-1:2004/A1:2008 - Eurocode 5: Design of timber structures – Part 1-1: General – Common rules and rules for buildings*. Brussels: CEN, 2008.

[21] CEN, *EN 1075:2015 - Timber structures - Test methods - Joints made with punched metal plate fasteners*. Brussels: CEN, 2015.

[22] CEN, *EN 1995-1-2: Eurocode5: Design of Timber Structures - Part1–2: General - Structural Fire Design.* Brussels: CEN, 2009.

[23] CEN, *EN 1381:2016 - Timber structures - Test methods - Load bearing stapled joints.* Brussels: CEN, 2016.

[24] CEN, *EN 26891:1991- Timber Structures - Joints made with mechanical fasteners - General principles for the determination of strength and deformation characteristics.* Brussels: CEN, 1991.

[25] J. Kunecký, V. Sebera, J. Tippner, and M. Kloiber, "Numerical assessment of behavior of a historical central european wooden joint with a dowel subjected to bending," in *SAHC2014 – 9th International Conference on Structural Analysis of Historical Constructions*, (Mexico City), 2014.

[26] J. Tippner, J. Milch, V. Sebera, J. Kunecký, M. Kloiber, and M. Navrátil, "Finite-element analysis of a historical truss reconstructed with a traditional all-wooden joints," in *SAHC2014 – 9th International Conference on Structural Analysis of Historical Constructions*, (Mexico City), p. 11, 2014.

[27] K. Šobra, *Static analysis of traditional carpentry joints.* PhD thesis, CTU in Prague, 2016.

[28] B.-H. Xu, A. Bouchaïr, M. Taazount, and P. Racher, "Numerical simulation of embedding strength of glued laminated timber for dowel-type fasteners," *Journal of Wood Science*, vol. 59, pp. 17–23, Feb. 2013.

[29] E. Šmídová and P. Kabele, "Constitutive Model for Timber Fracture under Tensile and Shear Loads," *Applied Mechanics and Materials*, vol. 784, pp. 137–144, Aug. 2015.

[30] H. Yoshihara and T. Satoh, "Examination of the off-axis tension test method for evaluating the shear properties of wood," *Forest Product Journal*, vol. 53, no. 5, pp. 75–79, 2003.

[31] T. Tannert, T. Vallée, S. Franke, and P. Quenneville, "Comparison of test methods to determine Weibull parameters for wood," *World Conference on Timber Engineering*, vol. 15, p. 19, 2012.

[32] B. Kasal and R. Blass, "Experimental and analytical investigation of crack development in composite reinforced laminated arch," *Materials and Structures*, vol. 46, pp. 173–180, Jan. 2013.

[33] B. Franke and P. Quenneville, "Analysis of the fracture behavior of Radiata Pine timber and Laminated Veneer Lumber," *Engineering Fracture Mechanics*, vol. 116, pp. 1–12, Jan. 2014.

[34] N. Yang and L. Zhang, "Investigation of elastic constants and ultimate strengths of Korean pine from compression and tension tests," *Journal of Wood Science*, vol. 64, pp. 85–96, Apr. 2018.

[35] E. Šmídová, P. Kabele, and M. Šejnoha, "Material parameters of European spruce for tensile-shear fracture modeling," *Engineering Structures*, vol. [In preparation], 2021.

[36] E. Šmídová, P. Kabele, and M. Šejnoha, "Finite element simulation of single edge notched timber arch," *Journal of Computational and Applied Mathematics*, vol. 400, no. 113676, p. 11, 2022.

[37] E. Šmídová and P. Kabele, "Comparison of failure criteria for wood in tensile-shear stress state," *Acta Polytechnica CTU Proceedings*, vol. 13, p. 115, Nov. 2017.

[38] F. P. Laboratory, *Wood handbook - Wood as an engineering material*. Forest Product Laboratory, Madison, Wisconsin, 2010.

[39] S. Franke, B. Franke, and A. M. Harte, "Failure modes and reinforcement techniques for timber beams – State of the art," *Construction and Building Materials*, vol. 97, pp. 2–13, Oct. 2015.

[40] E. Bartůňková, *Constitutive model of timber*. Master thesis, Czech Technical University in Prague, 2013.

[41] E. A. deSouza Neto, D. Peric, and D. R. J. Owen, "Finite strain implementation of an elastoplastic model for crushable foam," (Barcelona: CIMNE), Wiberg N-E, 1995.

[42] A. Hillerborg, M. Modeer, and P.-E. Petersson, "Analysis of crack formation and crack growth in concrete by means of fracture mechanics and finite elements," *Cement and Concrete Research*, vol. 6, no. 6, pp. 773–782, 1976.

[43] S. Weihe, B. Kröplin, and R. De Borst, "Classification of smeared crack models based on material and structural properties," *International Journal of Solids and Structures*, vol. 35, pp. 1289–1308, Apr. 1998.

[44] P. Helnwein, J. Eberhardsteiner, and A. Hanhijarvi, "Constitutive model for the short-term failure analysis of wood under multiaxial states of stress: Effect of radial compression," in *the First International Conference of the European Society for Wood Mechanics*, (Lausanne, Switzerland), Building Material Laboratory, Materials Science and Engineering Department, Swiss Federal Institute of Technology Lausanne (EPFL), 2001.

[45] S. W. Tsai and E. M. Wu, "A general theory of strength for anisotropic materials," *Journal of composite materials*, vol. 5, no. 1, pp. 58–80, 1971.

[46] P. J. Gustafsson, "Fracture Perpendicular to Grain - Structural Applications," in *Timber Engineering*, pp. 103–128, Chichester, England: John Wiley & Sons Ltd, 2003.

[47] P. J. Gustafsson, "Analysis of generalized volkersen-joints in terms of non-linear fracture mechanics," in *European Mechanics Colloquium 227: Mechanical Behaviour of Adhesive Joints*, (France), pp. 323–338, Pluralis, 1987.

[48] J. L. Jensen and P.-J. Gustafsson, "Shear strength of beam splice joints with glued-in rods," *J Wood Sci*, vol. 50, pp. 123–129, Apr. 2004.

[49] P. Glos, *Zur Modellierung des Festigkeitsverhaltens von Bauholz bei Druck-, Zug- und Biegebeanspruchung*. Berichte zur zuverlassigkeitstheorie der bauwerke, SFB 96, 1981. OCLC: 74503888.

[50] R. Hill, "A Theory of the Yielding and Plastic Flow of Anisotropic Metals," *Proceedings of The Royal Society A: Mathematical, Physical and Engineering Sciences*, vol. 193, pp. 281–297, Jan. 1948.

[51] S. Yamada and C. Sun, "Analysis of laminate strength and its distribution," *Journal of Composite Materials*, vol. 12, pp. 275–284, Oct. 1978. Publisher: SAGE Publications Ltd STM.

[52] Z. Hashin, "Failure criteria for unidirectional fiber composites," *Journal of Applied Mechanics*, vol. 47, pp. 329–334, June 1980.

[53] P. P. Camanho, "Failure criteria for fibre-reinforced polymer composites," *The World-Wide Failure Exercise*, p. 13, 2002.

[54] B. Kasal, *A nonlinear three-dimensional finite-element model of a light-frame wood structure*. PhD thesis, Oregon State University, USA, 1992.

[55] B. Kasal and A. Heiduschke, "Radial reinforcement of curved glue laminated wood beams with composite materials," *Forest Product Journal*, vol. 54, no. 1, pp. 74–79, 2004. OCLC: 833491626.

[56] P. L. Clouston and F. Lam, "Computational modeling of strand-based wood composites," *Journal of Engineering Mechanics*, vol. 127, pp. 844–851, Aug. 2001. Publisher: American Society of Civil Engineers.

[57] J. Cabrero, A. Heiduschke, and P. Haller, "Analytical assessment of the load-carrying capacity of axially loaded wooden reinforced tubes," *Compos Struct*, vol. 92, pp. 2955–2965, Nov. 2010.

[58] C. B. Norris, "Strength of orthotropic materials subjected to combined stresses," in *Miscellaneous Publication FPL-1816*, Madison, Wisconsin: Forest Products Laboratory, 1962.

[59] T. A. C. M. van der Put, "The tensorpolynomial failure criterion for wood," *Delft Wood Science Foundation Publication Series*, p. 31, Jan. 2005.

[60] B. Kasal and R. J. Leichti, "State of the art in multiaxial phenomenological failure criteria for wood members," *Progress in Structural Engineering and Materials*, vol. 7, pp. 3–13, Jan. 2005.

[61] J. Cabrero, C. Blanco, K. Gebremedhin, and A. Martín-Meizoso, "Assessment of phenomenological failure criteria for wood," *European Journal of Wood and Wood Products*, vol. 70, p. 12, Nov. 2012.

[62] S. Aicher and W. Klöck, "Linear versus quadratic failure criteria for inplane loaded wood based panels," *Otto-Graf-Journal*, vol. 12, p. 14, 2001.

[63] R. Hill, *The mathematical theory of plasticity*. Oxford Classic Texts in the Physical Sciences, Oxford, New York: Oxford University Press, Aug. 1998.

[64] R. L. Hankinson, "Investigation of crushing strength of spruce at varying angles of grain," in *Air Service Information Circular No. 259*, U.S. Air Service, 1921.

[65] C. Woodward and B. Clinton, *The elastic and strength properties of Douglas fir in the radial-longitudinal plane*. PhD thesis, New Mexico State University, New Mexico, 1986.

[66] P. B. Lourenco, R. De Borst, and J. G. Rots, "A plane stress softening plasticity model for orthotropic materials," *Int. J. Numer. Methods Eng.*, vol. 40, pp. 4033–4057, 1997.

[67] F. P. Kollmann and W. A. Cote, *Principles of wood science and technology: I Solid wood*. Berlin, Heidelberg: Springer Berlin Heidelberg, 1968. OCLC: 851389657.

[68] A. International, *ASTM D143-09 Standard test methods for small clear specimens of timber*. West Conshohocken: ASTM international, 2009.

[69] P. Clouston, *The Tsai-Wu strength theory for Douglas-fir laminated veneer*. PhD thesis, The University of British Columbia, Vancouver, 1995.

[70] ABNT, *NBR 7190: Projeto de estruturas de madeira*. Rio de Janeiro: ABNT, 1996.

[71] E. Winandy, "Wood properties," in *Encyclopedia of agricultural science*, pp. 549–561, San Diego: Academic Press, 1st ed., 1994.

[72] H. Reinhardt, H. Cornelissen, and D. Hordijk, "Tensile tests and failure analysis of concrete," *Journal of Structural Engineering*, vol. 112, no. 11, pp. 2462–2477, 1986.

[73] D. Pryl, "ATENA Program Documentation, Part 10, User Material DLL, Implementing a User Material Model," 2016.

[74] E. Šmídová and P. Kabele, "Constitutive model for timber fracture used for FE simulation of LVL arch," *APP*, vol. 15, pp. 109–113, Dec. 2018.

[75] "Ncorr downloads, http://ncorr.com/index.php/downloads, accessed 2021-6-13."

[76] "Ncorr_post: DIC post-processing tool, http://mech.fsv.cvut.cz/~nezerka/DIC/index.htm, accessed 2021-6-13."

[77] CEN, *EN ISO 527-2:1996 Plastics, Determination of tensile properties, Part 2: Test conditions for moulding and extrusion plastics*. Brussels: CEN, 1996.

[78] A. International, *ASTM E1820-09 Standard test method for determination of resistance to stable crack extension under low-constraint conditions*. West Conshohocken: ASTM international, 2010.

[79] H. T. Nguyen, M. Pathirage, G. Cusatis, and Z. P. Bažant, "Gap test of crack-parallel stress effect on quasibrittle fracture and its consequences," *Journal of Applied Mechanics*, vol. 87, p. 071012, July 2020.

[80] H. Nguyen, M. Pathirage, M. Rezaei, M. Issa, G. Cusatis, and Z. P. Bažant, "New perspective of fracture mechanics inspired by gap test with crack-parallel compression," *Proceedings of the National Academy of Sciences*, vol. 117, pp. 14015–14020, June 2020.

[81] A. Požgaj, D. Chovanec, S. Kurjatko, and M. Babiak, *Štruktúra a vlastnosti dreva*. Bratislava: Príroda, 1993.

[82] E. Karacabeyli and S. Gagnon, *Canadian CLT handbook*. Pointe-Claire, QC: FPInnovations, 2020.

[83] J. Vorel and P. Kabele, "Inverse analysis of traction-separation relationship based on sequentially linear approach," *Computers & Structures*, vol. 212, pp. 125–136, Feb. 2019.

[84] D. A. Hordijk, *Local approach to fatigue of concrete*. PhD. thesis, Delft University of Technology, Delft, The Netherlands, 1991.

[85] M. Vorechovsky and D. Novak, "Simulation of random fields for stochastic finite element analysis," in *Ninth International Conference on Structural Safety and Reliability*, (Italy), p. 8, 2005.

[86] A. F. Moshtaghin, S. Franke, T. Keller, and A. P. Vassilopoulos, "Random field-based modeling of size effect on the longitudinal tensile strength of clear timber," 2016. ISSN: 0167-4730 Num Pages: 9 Pages: 60-68 Volume: 58.